Construction and Building Materials 428 (2024) 136408

Contents lists available at ScienceDirect

Construction and Building Materials

journal homepage: www.elsevier.com/locate/conbuildmat

Valorization of biomass bottom ash in alkali-activated GGBFS-fly ash: Impact of biomass bottom ash characteristic, silicate modulus and aluminum-anodizing waste

Xuan Ling [a,b,*], Wei Chen [a], Katrin Schollbach [b], H.J.H. Brouwers [a,b]

[a] State Key Laboratory of Silicate Materials for Architectures, Wuhan University of Technology, Wuhan 430070, China
[b] Department of the Built Environment, Eindhoven University of Technology, PO Box 513, Eindhoven 5600 MB, the Netherlands

ARTICLE INFO

Keywords:
Biomass bottom ash
Alkali-activated materials
Anodizing waste
Leaching

ABSTRACT

Growing production of green energy from biomass has led to a surge in biomass bottom ash (BBA) generation, often relegated to landfills due to high leachable heavy metal content. This study proposed solidifying BBA in alkali-activated granulated ground blast furnace slag (GGBFS) and class F fly ash (CFA) blended binders. Investigations into the influence of BBA content, fineness, silicate modulus of activators, and aluminum-anodizing waste (AAW) on solidification performance were conducted, focusing on reaction mechanisms, phase assemblages, mechanical properties and leaching behavior. Results indicate relatively low reactivity of BBA and high leachable chloride (Cl^-), sulphate (SO_4^{2-}), chromium (Cr), molybdenum (Mo), lead (Pb) and zinc (Zn) contents from BBA. Increased BBA substitution leads to strength deterioration, while ground biomass bottom ash (GBBA) improves the mechanical performance slightly. This improvement is attributed to the increased reactive aluminosilicate content and an enhanced packing system resulting from finer particles. However, GBBA induces an increased heavy metals leaching. Higher silicate modulus activators enhance mechanical properties and reduce the leaching of Mo and Cl^-, while lower silicate modulus activator accelerates the reaction process, promoting the formation of hydrotalcite-like phases and reducing the leaching of Cr and SO_4^{2-}. Incorporating 0.5 wt% aluminum-anodizing waste improves immobilization efficiency of toxic ions, but further increases in dosage lead to higher leaching due to weakened mechanical performance. Overall, hybrid binders with 10 wt% G/BBA exhibit desirable mechanical properties, along with sufficient immobilization of leachable heavy metals, enabling their use as potential construction materials.

1. Introduction

In recent years, the promotion of renewable energy resources in the EU has led to an increase in the contribution of biomass fuels to the gross final energy consumption. Biomass fuels, known for being cost-effective and producing lower emissions during combustion, undergo thermal treatment, resulting in a significant reduction in volume and mass of biomass waste materials [1]. However, the surge in biomass usage has given rise to an elevated production of biomass ash (BA). According to Directive 2009/28/CE, approximately 15.5 million tons of BA waste are generated annually in the EU-27. Biomass fly ash (BFA) and bottom ash (BBA) are primary by-products derived from biomass incineration. BBA is the coarse fraction settling under the grate of the combustion chamber or incinerator [2,3], accounting for 60–90 wt% of the total ash generated in a grate furnace [4]. Compared to the traditional coal fly ash (CFA) and BFA, BBA typically contains lower levels of reactive SiO_2, Al_2O_3 and Fe_2O_3 [5]. Consequently, it is often directed to landfills. Nevertheless, BBA has been explored for civil engineering applications, serving as a filler in road embankments and substitutions for cement and aggregates in mortar/concrete formulations [2,6–8]. Previous studies have investigated the impact of substitution levels on the mechanical properties, shrinkage behavior and chloride penetration of the different cement/binder [6,8]. Notably, the chemical composition and reactivity of BBA vary based on biomass origin and the technological process applied in biomass thermal power plants (BTPPs) [1]. Despite containing highly leachable heavy metals (such as Pb, Cr, Zn, etc.), which pose environmental threats due to their long-term persistence, ecotoxicity, and bioaccumulation, the leaching behavior of BBA-modified blends has

---

[*] Corresponding author at: State Key Laboratory of Silicate Materials for Architectures, Wuhan University of Technology, Wuhan 430070, China.
E-mail address: X.ling@tue.nl (X. Ling).

https://doi.org/10.1016/j.conbuildmat.2024.136408
Received 3 January 2024; Received in revised form 9 April 2024; Accepted 23 April 2024
Available online 27 April 2024

been infrequently addressed [9].

The immobilization of heavy metals contaminated solid wastes using alkali-activated materials (AAMs) has garnered increasing research attention [10]. AAMs, fabricated through the polymerization of aluminosilicate precursors, are recognized as environmentally friendly and economical construction materials due to their lower CO_2 emission during the manufacturing and abundant precursor sources. Various industrial by-products, such as electric arc furnace dust, red mud, and bottom ash from coal power plants, have been successfully utilized in AAMs, effectively immobilizing the contained heavy metals [11–13]. The main proposed mechanisms for immobilizing heavy metals in AAMs system are as follows: a) Ion exchange of alkali metals during gel formation [14,15], e. g., divalent metal ions such as Zn^{2+} with a similar radius to Ca^{2+} can be exchanged in C-S-H gel. b) Covalent bonding of heavy metals to the aluminosilicate network [16], in which the negative charge of $[AlO_4]^-$ facilitates excellent immobilization of metal ions. c) Physical absorption by the gel products due to their high specific surface area [17]. d) Physical encapsulation in the AAMs matrix [18,19]. e) Precipitation in the form of hydroxides, carbonates and silicates [10]. It is crucial to keep in mind that immobilization efficiency often results from a combination of these mechanisms within a given system. Hence, understanding the leaching of heavy metals from BBA and their solidification in AAMs is pivotal and beneficial for the valorization of BBA in the civil engineering, advancing a more sustainable circular economy.

In accordance with the aforementioned mechanisms, the leaching behavior of the solidified units is highly influenced by the micro-scale matrix properties, regulated by several factors such as solid precursors [20], curing temperature [21], activator types and modulus [22], and additives e. g. calcined dolomite and layered double hydroxides [23,24]. Xu demonstrated the effect of activator modulus and GGBFS-CFA ratio on the reaction kinetics, hydrated gel structures and compressive strength of the blends, highlighting the advantages in mechanical properties with optimal parameters [20]. However, the solidification of BBA in such blends is expected to introduce variations in chemical composition and related properties. Therefore, a thorough understanding of the reaction process of BBA-GGBFS-CFA blends is crucial for optimizing the properties of the hybrid binders. Moreover, ingredient characteristics influence the mechanical performance of the blends. Komljenović et al. revealed that the compressive strength of alkali-activated fly ash is enhanced with the finer fly ash content [25]. Nevertheless, limited attention has been given to the BBA fineness, despite its significant impact on the dissolution process, particle packing in the matrix, and the leaching capacity of heavy metals. Therefore, understanding the role of BBA fineness is vital for optimizing the strength and leachability trade-off in the BBA-GGBFS-CFA blends.

Aluminium-anodizing waste (AAW) is a by-product generated during the aluminium anodizing process in the aluminium industry. Substantial quantities of AAW are systematically collected in local wastewater treatment plants situated in the Netherlands. It primarily consists of aluminium hydroxide with various polymorphisms, such as bayerite and boehmite. Due to the presence of heavy metals such as Cr and Ni, much of this waste is disposed of through sewage systems or landfills after undergoing prior treatment. In an effort to enhance the recycling of this aluminium-rich material, Correia et al. conducted an investigation into its potential application as coagulant in municipal wastewater treatment [26]. Furthermore, AAW has been identified for prospective utilization in diverse applications, including refractory materials [27,28], insulation panels [29], ceramic filters [30] and bricks [31]. Notably, recent attention has been directed towards its utilization in the production of hydraulic binders. Souza et al. elucidated that AAW exhibits promise as a shrinkage-compensating admixture when combined with Portland cement, attributed to the promoted formation of ettringite [32]. Additionally, AAW has been suggested as a viable component in the manufacturing process of calcium sulphoaluminate cements via the hydrothermal calcination method [33,34]. However, to the best of our knowledge, there are few studies that investigate the application of AAW in AAMs, despite the fact that aluminosilicates are the reaction precursors of AAMs. This study aimed to utilize the high aluminium content in AAW to effectively modify the resulting reaction products. Based on the feature that the negative charge of tetrahedral $[AlO_4]^-$ in the gel chains enhances the immobilization of metal ions as previously mentioned, the possibility of synergistic treatment of AAW and BBA in AAMs has been explored in the present study to improve the solidification efficiency of heavy metals and to achieve the concept of multiple waste reuse.

Based on the above considerations, the primary objective of this study is to solidify BBA in AAMs to render it as a construction material, thereby leveraging the advantages of AAMs instead of resorting to landfilling. Given the complexity of the AAMs matrix, the interaction between AAMs and BBA, as well as the resulting immobilization efficiency, are expected to vary. The study investigates the influence of BBA content, fineness, silicate modulus (Ms) of activators, and AAW on the solidification process, focusing on the reaction mechanism, phase assemblages, mechanical properties and leaching behavior. The findings of this study contribute to establishing a theoretical foundation, feasibility assessment, and principles of the selection of raw materials and additives for the solidification of BBA.

2. Experimental program

2.1. Materials

Granulated ground blast furnace slag (GGBFS), Class F coal fly ash (CFA), Biomass bottom ash (BBA) and Aluminum-anodizing waste (AAW) were used as the raw materials in this study. GGBFS was provided by HeidelbergCement (ENCI), IJmuiden, Netherlands. CFA was purchased from Vliegasunie, Netherlands. BBA and AAW were provided by Eurotrust Management, Netherlands. The BBA was originally collected from a local bio-power plant that utilized a grate furnace and a steam boiler for energy production. The plant burned B-wood, classified by the Ministry of Infrastructure and the Environment, Netherlands, which includes painted and glued wood, as well as wood-wool composite boards [35]. Notably, the received BBA contained some charcoal fragments (5 wt%) as shown in Supplementary Figure S1(a), which had larger particle sizes exist in the received BBA. To prevent any adverse effects of the charcoal fragments on the mechanical properties of the blends [36], the received BBA was initially sieved for homogeneity, reducing it to below 1 mm as depicted in Supplementary Figure S1(b). To reveal the influence of BBA fineness on the blends, the BBA was then ground for 5 min at 250 rpm in a ball mill, resulting in the production of ground BBA powder as shown in Supplementary Figure S1(c), hereinafter referred to as GBBA. AAW was collected from a local wastewater treatment plant where aluminium was removed from the sewage using electrodialysis technology. The received AAW was dried at 60 °C to remove the free water and subsequently ground for 1 min at 250 rpm for further characterization and application.

The particle size distribution of raw materials was determined using a laser light scattering technique (Mastersizer 2000, Malvern), and the results are presented in Fig. 1. The average particle size (d50) of GGBFS, CFA, BBA, GBBA and AAW is found to be 13.3 μm, 14.0 μm, 125.5 μm, 30.0 μm and 5.8 μm respectively. The particle size of BBA is larger compared to that of CFA and GGBFS, while GBBA exhibits a similar particle size. It should be noted that longer grinding times and higher speeds would result in finer particles. However, this would also lead to increased costs and time requirements in the pre-treatment process. Therefore, the effect of both milled and un-milled BBA on its solidification performance is considered in the present work. The chemical composition of raw materials was determined by X-ray fluorescence spectrometry (XRF) (PANalytical Epsilon 3). The borate fusion method was used for the preparation of fused beads. The chemical composition of the raw materials is given in Table 1 in the form of oxides, along with the specific density and the Blaine specific surface area (as per European

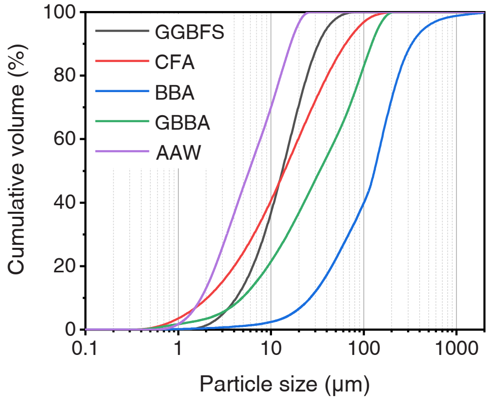

Fig. 1. The particle size distribution of raw materials.

Table 1
Chemical and physical properties of raw materials.

The substituent (%)	GGBFS	CFA	BBA	GBBA	AAW
CaO	38.6	6.1	17.3	17.1	1.0
SiO_2	31.2	54.6	48.9	49.6	0.8
Al_2O_3	13.1	21.6	6.2	7.5	55.2
Fe_2O_3	0.7	9.0	3.0	2.6	0.6
K_2O	0.3	2.9	1.9	2.1	-
P_2O_5	-	-	1.3	1.2	0.2
Na_2O	-	-	-	-	4.2
SO_3	5.2	0.4	2.9	2.6	11.8
MgO	9.0	1.2	2.9	2.5	-
TiO_2	1.3	-	3.6	3.2	-
Cr_2O_3	-	-	0.1	0.1	-
ZnO	-	-	0.5	0.5	-
PbO	-	-	0.1	0.1	-
Others	-	2.1	3.9	3.6	2.4
LOI	0.6	2.1	7.4	7.3	23.8
Specific density (g/cm^3)	2.90	2.14	2.87	2.89	2.54
Blaine specific surface area (m^2/kg)	460	325	165	295	490

standard EN 196–6). For the preparation of the activating solution with various Ms (1.0, 1.4, 1.8), commercial sodium silicate solution procured from Labshop (Mass ratio: 26.9% SiO_2, 8.0% Na_2O, 65.1% H_2O) and sodium hydroxide pellets (97%, Sigma-Aldrich) were used in combination with distilled water.

2.2. *Mixture design and specimen preparation*

The reference blend (70 wt% GGBFS and 30 wt% CFA) was activated using sodium silicate solution (Ms = 1.4, Na_2O = 5.6 wt%). Different proportions of CFA were replaced with 33.3, 66.6 and 100 wt% BBA, corresponding to 10, 20 and 30 wt% of the total binder, respectively. The water-to-binder (w/b) ratio was maintained at 0.4 for the pastes based on the previous study on the alkali-activated slag and fly ash blends [37]. A higher w/b ratio of 0.45 was employed for the mortars to accommodate the water demand of the fine aggregates [38]. Notably, free water from the original sodium silicate solution was included in the calculation of the w/b ratio. Activator solutions with Ms of 1.0,1.4 and 1.8 were used to assess the influence of active [SiO_2] contents on the performance of the blended systems. The activating solution was naturally cooled to ambient temperature for 24 h before mixing. Furthermore, the role of BBA fineness was studied using 10 wt% and 20 wt% GBBA. The effect of additional AAW content (0.5 wt% to 2.5 wt%) was investigated in the groups with 10 wt% GBBA. Detailed information on mix proportions and flowability can be found in Table 2. Compared with the spherical shape of CFA particles, the angular shape of BBA and AAW particles results in a larger surface area and higher water demand. Therefore, increasing the dose of BBA and AAW decreases their flowability.

Paste and mortar samples were prepared for micro-scale and mechanical properties analyses. The paste samples were mixed using a laboratory mixer. The binder materials were first mixed for 1 min to reach a homogeneous state, followed by the addition of activating solution. After stirring the bottom specimens for 30 s, then further mixed for another 120 s at a medium speed. The fresh paste was then cast into plastic molds of 40 × 40 × 160 mm^3 and vibrated for 1 min. A plastic film was applied to the top surface for 24 h curing. Finally, all specimens were demolded and cured at 20 $\pm$ 1°C with a relative humidity of 95% until the testing age. For the mortar samples, the corresponding standard sand was added during the stirring and the sand/binder ratio was set as 3 according to EN 196–1:2016.

2.3. *Methodology*

2.3.1. *Reactivity analysis of raw materials*

The reactivity of BBA, GBBA and AAW was evaluated by subjecting them to a high alkali concentration solution. Previous studies have established that an 8 M NaOH solution is adequate for activating of fly ash and metakaolin [39,40]. Luo et al. utilized an 8 M NaOH solution to investigate the reactivity of the ladle slag, a by-product of the steelmaking process [41]. Accordingly, an 8 M NaOH solution was employed in the present study, with a liquid-to-solid (L/S) ratio of 50 to ensure a sufficient reaction. 20 g dry materials and alkaline solution were mixed in the sealed polyethene bottles and placed horizontally on a linear reciprocating shaking device (Stuart SSL2) at a constant rate of 250 rpm with an amplitude of 20 mm for 24 h. Then the residual was collected by filtering with 0.45 μm paper and washed with deionized water. After 24 h vacuum drying at 60 °C, the residual mass was recorded, and its chemical and phase composition were characterized with XRF and XRD

Table 2
The proportion of each material and flowability in the designed mixtures (%) (Na_2O wt% = 5.6).

ID	GGBFS	CFA	BBA	GBBA	AAW	Ms	w/b	Sand	Flowability (mm)	Setting time (min)
R0–1.4	70	30	0	/	/	1.4	Paste =0.4 Mortar =0.45	300	261	36/82
R10–1.4		20	10	/	/	1.4			223	32/76
R20–1.4		10	20	/	/	1.4			191	28/72
R30–1.4		0	30	/	/	1.4			157	26/70
R10–1.0		20	10	/	/	1.0			215	28/70
R10–1.8		20	10	/	/	1.8			228	36/82
R20–1.0		10	20	/	/	1.4			175	24/66
R20–1.8		10	20	/	/	1.8			198	32/78
G10–1.4		20	/	10	/	1.4			249	30/76
G20–1.4		10	/	20	/	1.4			224	28/70
G10A0.5		20	/	10	0.5	1.4			219	32/80
G10A1.5		20	/	10	1.5	1.4			189	38/86
G10A2.5		20	/	10	2.5	1.4			150	40/96

Note: G10–1.4 is also used as G10A0 in the comparison of additional AAW, and Ms is silicate modulus, initial/final setting time.

tests (see Section 2.3.5). The calculation of reactive elements is described in Supplementary Text S1. Additionally, a similar treatment was performed on GBBA in distilled water to reveal its dissolution behavior.

2.3.2. *Isothermal calorimeter*

The reaction kinetics of the blends were determined by an isothermal calorimeter (TAM Air, Thermometric). The raw materials were initially mixed according to the paste mixture. Then the activating solution was added for around 1 min vibration using an electrical vibrator. The mixed paste was injected into a sealed ampoule and loaded into the calorimeter. The heat release and heat flow results were normalized by the mass of the solid binder. The measurement was conducted for the first 160 h at a temperature of 20 ± 0.2°C.

2.3.3. *Workability and compressive strength*

The mini spread flow table test was conducted to determine the flowability of the fresh mortars according to EN 1015–3:2007. The fresh mortar was introduced into a truncated conical mould (60 mm in height, 100 mm in diameter at the bottom, and 70 mm in diameter at the top). After raising the mould vertically, the mortar was spread onto the disc by jolting the flow table 15 times. The diameter of the mortar in two perpendicular directions was then measured. The compressive strength of the mortar after 7d, 28d curing was measured according to EN 196–1:2016. A loading rate of 2400 N/s was applied to six specimens for each mixture. The obtained average value was recorded as the compressive strength value.

2.3.4. *Leaching test of raw materials and hydrated samples*

The one-batch leaching test was performed with raw materials and 28 d paste samples (EN 12457–1:2002). The paste samples were crushed and milled into powders (0.125 ~ 1 mm), then mixed with distilled water in a polyethene bottle with a liquid-to-solid (L/S) ratio of 10. Afterwards, a similar shaking process was conducted with the sealed bottle on the Stuart SSL2 for washing at a constant rate of 250 rpm for 24 h. The solids were then filtered out, and the pH of the leachate was measured. The element analysis was then carried out with inductively coupled plasma optical emission spectroscopy (ICP-OES Spectral Blue) and ion chromatograph (IC, Dionex 1100). The calculation of the leachable elements is described in Supplementary Text S2.

2.3.5. *Phase assemblage analysis of raw materials and hydrated samples*

The phase composition of the blended paste samples was analyzed by X-ray diffraction (XRD), Thermogravimetry (TG), and Fourier transforms infrared spectroscopy (FT-IR). XRD characterization as performed on raw materials, the residual BBA after the reactivity test, and the hydrated assemblages. The test was carried out with a step size of 0.02° and a 2θ range from 10° to 60° (40 kV, 30 mA) by using a Bruker D4 phaser equipped with a Co X-ray tube. The PDF numbers of the identified phases are provided in Supplementary Table S1. The TG test was performed on the hydrated samples by a STA 449 F1 instrument test at a heating rate of 10 K/min up to 1000 °C under the N_2 atmosphere. The Fourier-transform infrared (FT-IR) spectrum of samples was conducted using a Varian 3100 instrument to identify the bonding in the mineral phases. All samples were scanned 15 times at a resolution of 1 cm^{-1} with a wavenumber range of 4000–400 cm^{-1}. To facilitate the identification of distinct bands and differentiate between wavenumbers, the second derivative of the measured transmittance (%) over the wavelength (cm^{-1}), denoted as d^2T/dW^2, was employed [42,43].

2.3.6. *Mercury intrusion porosimetry (MIP) analysis of hydrated samples*

MIP analysis was performed to characterize the pore structure of the blends by using a mercury porosimeter (AutoPore IV 9500, Micromeritics). The hardened 28d pastes were crushed into around 4 mm granular pieces and then immersed in isopropanol to terminate the hydration. The pieces were vacuum dried at 40 °C for 24 h before the test.

3. Results

3.1. *Reactivity of BBA, GBBA and AAW*

The reactive content within BBA, GBBA and AAW was assessed under conditions of high alkalinity solution, wherein minerals might undergo dissolution, and new reaction products could precipitate. Therefore, the mineralogical composition of raw materials was characterized both before and after the reaction. The results for GBBA are presented in Fig. 2, while Supplementary Figure S2 illustrates the corresponding findings for BBA. The raw BBA and GBBA primarily consist of quartz (SiO_2), anhydrite ($CaSO_4$), microcline ($K_2O{\cdot}Al_2O_3{\cdot}6SiO_2$), rutile ($TiO_2$), calcite ($CaCO_3$), lime (CaO) and smaller proportion of other minerals such as gehlenite ($2CaO{\cdot}Al_2O_3.SiO_2$) and calcium titanium oxide ($CaTiO_3$). Significantly, certain minerals like anhydrite have shown susceptibility to dissolution, a fact supported by the XRD pattern analysis of the residues in distilled water (refer to). These observations are further corroborated by the changes observed in the chemical composition, as demonstrated in Supplementary Table S2, wherein notable reductions in CaO and SO_3 levels are evident subsequent to the dissolution process in distilled water.

After 24 h of reaction with 8 M NaOH solution, 17.6 g of residues remained for BBA, and 17.2 g of residues for GBBA. The dissolution of anhydrite and lime was also observed during this process, as evidenced by the disappearance of associated peaks in the XRD patterns. Significantly, a higher mass loss in GBBA indicates an enhanced reactive content due to the milling process, as corroborated by the elevated reactive content of Ca, Al and Si as presented in Table 3. Furthermore, traces of hydrotalcite-like phases ($Mg_6Al_2CO_3(OH)_{16}4H_2O$) are discernible around 13° (2θ, Co Kα) in both GBBA and BBA residues. In summary, BBA inherently possesses a certain amount of reactive content, contributing to the formation of hydrotalcite-like phases. The milling process of BBA further amplifies the reactive content within GBBA.

In the case of AAW, no residues were detected after the reaction in the high alkali solution. Given that the raw AAW comprises low-crystallinity boehmite (AlOOH), bayerite ($Al(OH)_3$), and thenardite (Na_2SO_4) (see detailed XRD pattern in Section 3.5), the reaction process is elucidated by Eq.1 and Eq. 2 [44,45]. The high reactivity of [AlO_4] in AAW designates it as the aluminum source for the formation of aluminum-containing phases, including hydrotalcite-like compounds

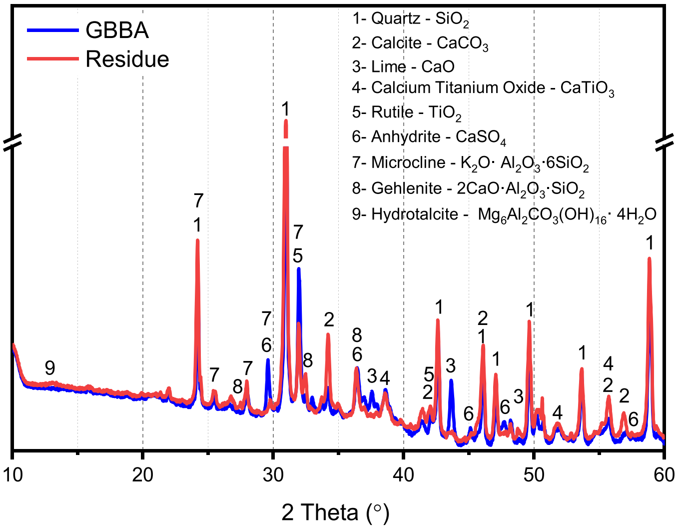

Fig. 2. XRD pattern of the raw GBBA and the residue GBBA after 24 h reactive test in 8 M NaOH solution. (Legend: 1- Quartz, 2- Calcite, 3- Lime, 4- Calcium titanium oxide, 5- Rutile, 6- Anhydrite, 7- Microcline, 8- Gehlenite, 9- Hydrotalcite).

Table 3

The chemical composition of the BBA/GBBA and residue BBA/GBBA after 24 h reactive test in 8 M NaOH solution.

Oxide (%)	MgO	Al_2O_3	SiO_2	P_2O_5	SO_3	K_2O	CaO	TiO_2	Fe_2O_3	Others	Mass (g)
BBA	2.9	6.2	48.9	1.3	2.9	1.9	17.3	3.6	3.0	4.6	20.0
Residue	2.7	5.5	47.1	1.1	0.1	1.3	14.4	3.3	3.0	4.0	17.6
Change	0.2	0.7	1.8	0.2	2.8	0.6	2.9	0.3	0.0	0.6	
GBBA	2.5	7.5	49.6	1.2	2.6	2.1	17.1	3.2	2.6	4.3	20.0
Residue	2.1	6.1	46.5	1.0	0.0	1.4	14.6	2.8	2.4	3.7	17.2
Change	0.3	1.4	3.1	0.2	2.6	0.8	3.5	0.4	0.2	0.6	

Note: all the chemical composition of the residue BBA/GBBA is normalized with the unreacted BBA/GBBA.

and C-A-S-H gels.

$$AlOOH + OH^- + H_2O \rightarrow Al(OH)_4^- \quad (1)$$

$$Al(OH)_3 + OH^- \rightarrow Al(OH)_4^- \quad (2)$$

3.2. Reaction kinetics of BBA-GGBFS-CFA blends

Fig. 3 illustrates the hydration kinetics of all blends within the initial 160 h. The heat flow, normalized by the dry solid of the blended binder (with 10, 20 and 30 wt% BBA and the Ms = 1.4 of activator solution), is presented in Fig. 3 (a). The reaction process of alkali-activated materials generally includes four stages: dissolution, induction, acceleration and stable period [21,46]. The initial heat release from the dissolution of solid precursors is not depicted in the present results [47]. After that, a higher replacement level of BBA diminishes the intensity of heat flow peaks, indicating reduced heat release compared to R0–1.4. However, 10 wt% BBA exhibits the highest normalized cumulative heat within 168 h, suggesting its positive impact on reactivity. Considering that CFA has a relatively low influence on the reaction at an early age [38], substituting it with BBA does not lead to a significantly reduction in heat release. Instead, the dissolution of minerals (lime and anhydrite) in BBA particles enhances the reactive [Ca^{2+}] content, promoting the formation of C-(A)-S-H gel at an early age.

In Fig. 3 **(b)**, when alkali solutions with various Ms are applied to blends containing 10 wt% and 20 wt% BBA, a higher Ms of the activator extends the induction stage and reduces the intensity of the primary heat flow peak. The increase in the SiO_2/Na_2O ratio in the activator leads to a drop in the alkalinity [48], thereby slowing down the dissolution of the solid precursors. A similar trend is observed in samples with 20 wt% BBA, where a lower Ms of the activator accelerates the reaction process.

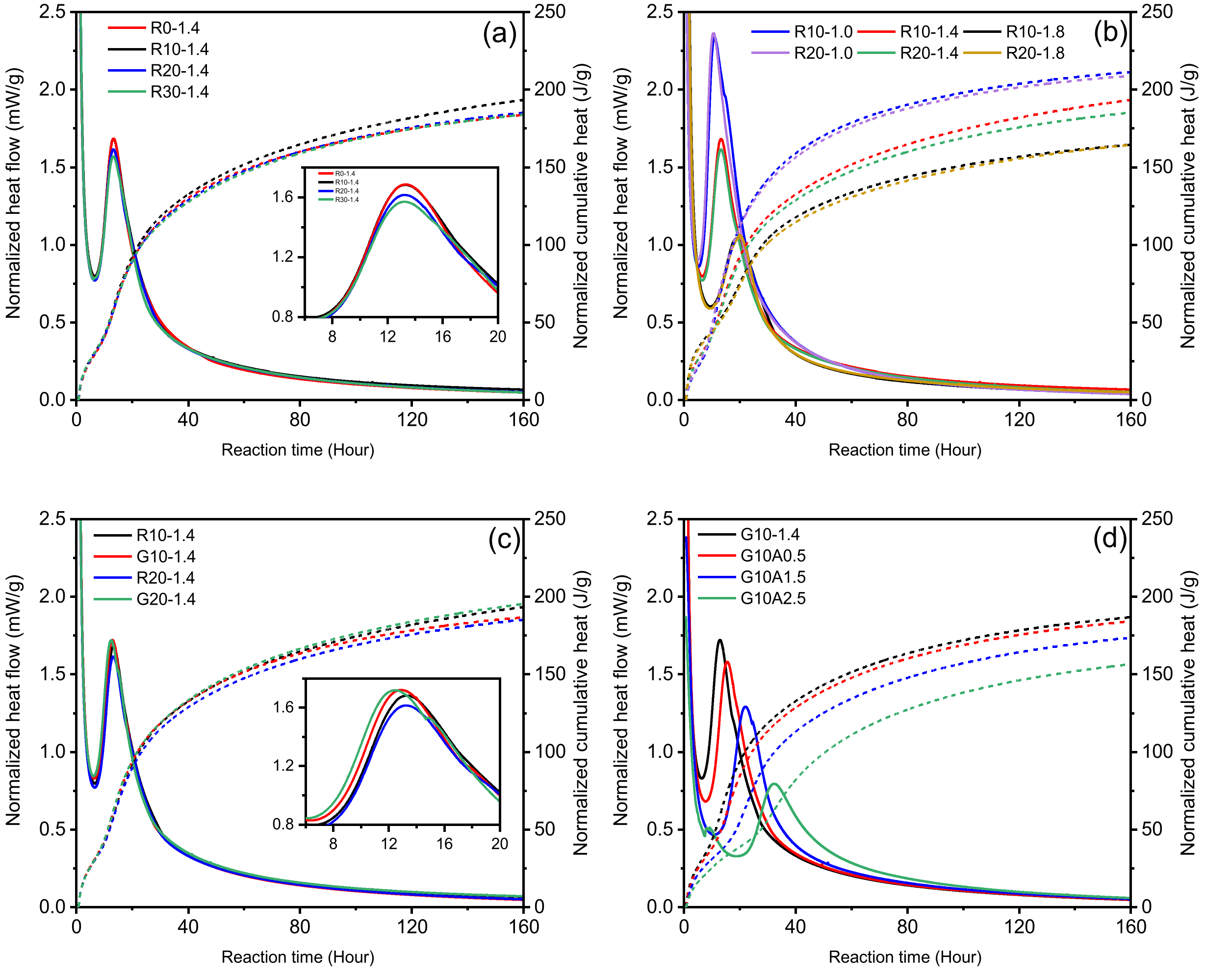

Fig. 3. Normalized heat flow and cumulative heat flow of the blends within 7d (a): replacement levels of BBA, (b): silicate modulus, (c): particle size of BBA, (d): additional AAW.

In Fig. 3 **(c),** the substitution of BBA with GBBA slightly promotes the reaction due to the finer particles, which facilitate the dissolution of lime and anhydrite, resulting in an increased release of reactive [Ca^{2+}] and accelerated hydration. Moreover, GBBA contains higher reactive Al_2O_3 and SiO_2 content compared to BBA, as outlined in Section 3.1, contributing to the gel formation and further augmenting the cumulative heat. Conversely, the presence of additional AAW in Fig. 3 **(d)** retards the reaction process by consuming alkaline ions and reducing the alkalinity of the reaction environment.

Overall, the replacement of CFA by BBA does not significantly impact the reaction behavior, suggesting the feasibility of using BBA in blends from the perspective of the reaction process. Meanwhile, the reaction process can be regulated by adjusting the Ms of activator and AAW content, with the finer BBA particles slightly enhancing the reaction.

3.3. Phase assemblage

3.3.1. XRD analysis

The XRD patterns depicted in Fig. 4 **(a)** illustrate the raw materials mineralogical composition, while Fig. 4 **(b-d)** offers a comparative analysis of the XRD patterns for all 28d samples. In the case of R0–1.4, the main crystalline phases identified include mullite ($Al_{4.8}O_{9.6}Si_{1.2}$), quartz (SiO_2), and calcite ($CaCO_3$), originating from raw CFA. The broad peaks around 34.2°(2θ) indicates the formation of amorphous C-(A)-S-H gel, which is considered as the main reaction products in AAMs [49]. For BBA-substituted samples (Fig. 4 **(b)**), in addition to the phases observed in R0–1.4, traces of rutile (TiO_2) and calcium titanium oxide ($CaTiO_3$) originating from BBA are detected. Notably, minor peaks indicative of hydrotalcite-like phases are observed. As the BBA content increases, there is a corresponding augmentation in the intensity of these hydrotalcite-like phase peaks, suggesting the active involvement of BBA in their formation. In the GBBA-substituted samples G10–1.4 and G20–1.4, no substantial difference in crystalline phases is discernible when compared with the R10–1.4 and R20–1.4. This observation can be attributed to the similar chemical composition between GBBA and BBA.

When various activators are applied to the blends (Fig. 4 **(c)**), discernible differences primarily manifest in the intensity of peaks corresponding to hydrotalcite-like phases and C-(A)-S-H gels. Activator with lower Ms exhibit heightened intensity, attributable to increased alkalinity accelerating the reaction process of the blends, as described in the reaction kinetics in Section 3.2. Consequently, an augmented formation of hydrotalcite-like phases and C-(A)-S-H gels at 28d is anticipated in R10–1.0 and R20–1.0. Notably, the lower proportion of SiO_2 in the activator directs a greater involvement of $Al(OH)_4$ in solution toward the formation of hydrotalcite-like phase rather than the formation of C-(A)-S-H gel [51].

In Fig. 4 **(d)**, the incorporation of AAW into the blends is depicted, revealing no discernible new crystalline phase apart from those detected in G10–1.4. In summarize, the main hydration products, including the hydrotalcite-like phase and C-(A)-S-H gel, persist regardless of BBA modification, activator modulus, and the introduction of additional AAW. In general, the hydrotalcite and related layered double hydroxides

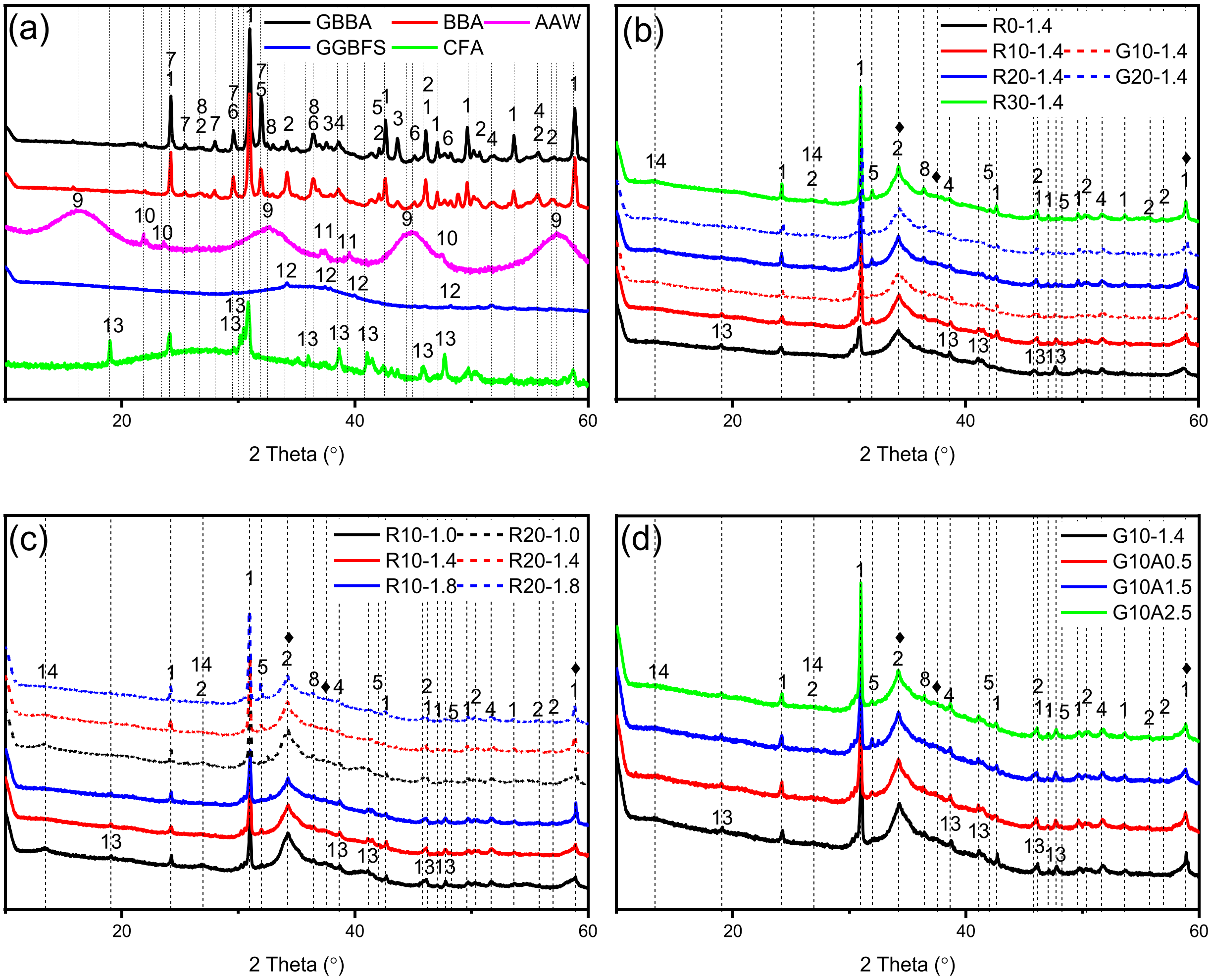

Fig. 4. XRD patterns of 28 d samples (Legend: 1- Quartz, 2- Calcite, 3- Lime, 4- Calcium titanium oxide, 5- Rutile, 6- Anhydrite, 7- Microcline, 8- Gehlenite, 9- Boehmite, 10- Bayerite, 11- Thenardite, 12- Hatrurite, 13- Mullite, 14- Hydrotalcite, ◆-C-(A)-S-H gel [50]).

(LDHs) phases demonstrate the capacity for ion immobilization [52], making them widely application in waste management [53]. The impact of these products on the leaching characteristics of the BBA-GGBFS-CFA system will be further addressed in Section 3.5.

3.3.2. *FT-IR analysis*

In addition to the formation of hydrotalcite-like phase, the gel products exhibit the capacity to adsorb the heavy metals on the surface and interlayer region [54,55]. Therefore, the impact of BBA content, fineness, activator modulus and additional AAW on gel characteristics was investigated using FT-IR, as depicted in Fig. 5. The FT-IR spectra of raw materials are presented in Fig. 5 **(a)**. Two adsorption peaks are observed for raw GGBFS. The major band at around 900 cm^{-1} and 500 cm^{-1} corresponds to the asymmetric stretching vibration of Si-O-T bonds (T represents tetrahedral Si or Al units) [56]. The same vibration for CFA is shifted to around 1020 cm^{-1} due to the slightly different composition of the amorphous phase in the raw materials [57]. Bands at about 795 cm^{-1}, 776 cm^{-1} and 555 cm^{-1} confirms the presence of mullite and quartz in CFA [58]. For BBA and GBBA, the main adsorptions at 1418 cm^{-1} and 875 cm^{-1} are related to O-C-O bonds of carbonates [59], while the weak peaks at 612 cm^{-1} and 592 cm^{-1} are attributed to the vibrations of S-O from the anhydrite. AAW shows the bands around 3326 cm^{-1}, 1075 cm^{-1} and 482 cm^{-1}, corresponding to the O-H and Al-O vibrations from bayerite and colloidal boehmite. In Fig. 5 **(b)**, which showcases the modified samples, all FTIR spectra show absorption bands around 3370 cm^{-1}, 1660 cm^{-1}, 1415 cm^{-1} and 950 cm^{-1}. These bands are associated with the stretching and bending vibration of H-O bonds, stretching vibration of O-C-O bonds in carbonates, and the asymmetric and symmetric stretching vibration of Si-O-T bonds in [SiO_4] and [AlO_4], respectively [42].

The impact of BBA contents, fineness, Ms of activators and additional AAW on the structure of C-(A)-S-H gel is explored in Fig. 5 **(c)** within a wavenumber range of 1200 – 600 cm^{-1}, recognized as a characteristic region for aluminosilicates [50]. The primary band centered around 950 cm^{-1} is commonly ascribed to Q^2 silica units within the C-(A)-S-H gel [60,61]. Notably, recent studies have posited that bands around 930 cm^{-1} and 1060 cm^{-1} may also contribute to Q^2- silicate species [62, 63]. However, these potential adsorptions associated with Q^2-silicate is observed at 910 cm^{-1} in the BBA-GGBFS-CFA system, indicating a distinct degree of gel polymerization in AAMs compared to ordinary Portland cement. The signal at 810 cm^{-1} corresponds to Si-O stretching of Q^1 tetrahedra [42], and the signal at 665 cm^{-1} is related to Si-O-Si bending vibrations [64]. The band at about 890 cm^{-1} has been correlated with the stretching vibration of Al-O-Si [65], while the band at 1050 cm^{-1} is associated with the symmetric bending of Al-O-H [42]. When BBA is incorporated, the intensities of Q^2 decrease with higher BBA content, particularly evident in R30–1.4, indicating shorter silica chains due to the release of more Ca^{2+} from the BBA. A similar decline is observed in the bands around 890 cm^{-1}, indicating less substitution of [AlO_4] in C-(A)-S-H gel due to lower reactive aluminum content in BBA compared to CFA.

In comparison to BBA, the utilization of finer GBBA slightly enhances the intensity of Q^2 and the Al-O-Si bond owing to the presence of more reactive silicate and aluminum caused by the enhanced dissolution of the finer particles. These elements promote the polymerization of silica chains and the substitution of [SiO_4] in the Q^2 sites by [AlO_4]. A similar intensified Q^2 bond is observed when a smaller Ms activator is employed. Interestingly, despite the lower [SiO_2] content provided by the low Ms activator solution, heightened alkalinity enhances the dissolution of silicates from solid precursors, facilitating increased involvement in gel formation. This observation also aligns with the promoted heat of hydration, as discussed in Section 3.2. Furthermore, an enhanced Al-O-Si bond is observed, particularly in the low Ms activator, where the higher alkalinity also reinforces the dissolution of CFA and BBA particles, leading to an enhanced substitution of [AlO_4] in C-A-S-H gel.

Regarding the addition of AAW, no significant increase in the Al-O bond around 1075 cm^{-1} is observed, indicating sufficient dissolution of AAW in the system. The slightly growing absorption peak ascribed to the Si-O-Al bridge with increasing AAW confirm that [AlO_4] generated by AAW actively participates and displaces the Si-O-T tetrahedra within the gel. This process results in a negative charge within the gel, proving highly favorable for the adsorption and immobilization of heavy metals in the gel matrix [16]. To summary, the outlined modifications, including grinding, lower Ms of activators, and additional AAW, can improve the incorporation of [AlO_4] in the gel products, which is beneficial for the solidification of heavy metals and ions within the matrix.

3.3.3. *TG-DTG analysis*

Thermogravimetric analysis was conducted on all 28d samples, and the results are depicted in Fig. 6.The main mass loss peak (50 °C to 250 °C) is attributed to the dehydration of bound water from the C-(A)-S-H gel [66,67]. The shoulder around 250 °C and the broad peak around 400 °C in the DTG curves are associated with the dehydration of hydrotalcite-like phases [68]. Additionally, the decomposition of carbonates is observed at approximately 650 °C. While these carbonates mainly originate from raw materials, it is possible that some additional carbonates formed during the curing and preparation. Furthermore, a minor mass loss peak that occurs around 800 °C is related to the decomposition of C-(A)-S-H gel to wollastonite ($CaSiO_3$) [69].

To evaluate the quantity of reaction products, the mass loss attributed to dehydration was calculated using a tangential method and is presented in Table 4 [70]. Comparing with R0–1.4, it is evident that the bound water content from gels decreases in the blends with BBA/GBBA substitutions, various activators and AAW additives. This decrease suggests a lower formation of C-(A)-S-H gel in the modified paste due to the replacement of CFA. It is important to note that the mass loss due to the dehydration of C-(A)-S-H gels overlaps with the dehydration of the hydrotalcite-like phases, making their separation difficult and potentially leading to deviations in the calculated bound water content of the gels. However, R0–1.4 exhibits the lowest bound water content between 250 °C to 500 °C, confirming the reduced formation of hydrotalcite-like phases in the referenced blend. In other words, after the modifications, more free water is bound in hydrotalcite-like phases, especially in samples with Ms of 1.0, aligning with the XRD patterns in Fig. 4 **(c)**. Regarding the AAW modified samples, there is less bound water in the gels, indicating that the reduced alkalinity weakens the gel formation due to the dissolution of AAW. However, it should be noted that the $Al(OH)_4^-$ contributes to the formation of hydrotalcite-like phases owing to the increase of $Al(OH)_4^-$ in the solution. In summary, the use of BBA/GBBA, activators with lower Ms, and additional AAW can promote the consumption of free water in the reaction system by forming hydrotalcite-like phases.

3.4. *Microstructure*

The microstructural properties of the modified samples are associated with the physical encapsulation effect of heavy metals. MIP analysis of 28d samples was performed and the results are demonstrated in Fig. 7 **(a-d)**. Pores in cementitious materials are typically classified as gel pores (< 10 nm), capillary pores (10–5000 nm) and macro-pores (> 5000 nm) [71]. The total porosity and the porosity of various size pores are summarized in Fig. 7 **(e)**. Among the tested samples, R0–1.4 exhibits the lowest porosity of 3.5%, while the modifications increase the total porosity. This increase is mainly attributed to reduced workability after the incorporation of BBA/GBBA (Table 2), resulting in more capillary and macro-pores. Nevertheless, the substitution of BBA promotes the gel pores, which is consistent with the increased amount of bound water from the C-(A)-S-H gel (Table 4). as demonstrated by Wang et al., that the C-(A)-S-H gels with a higher Ca/Si ratio exhibit increased porosity and surface area [15]. Hence, the release of more soluble Ca^{2+} ions from

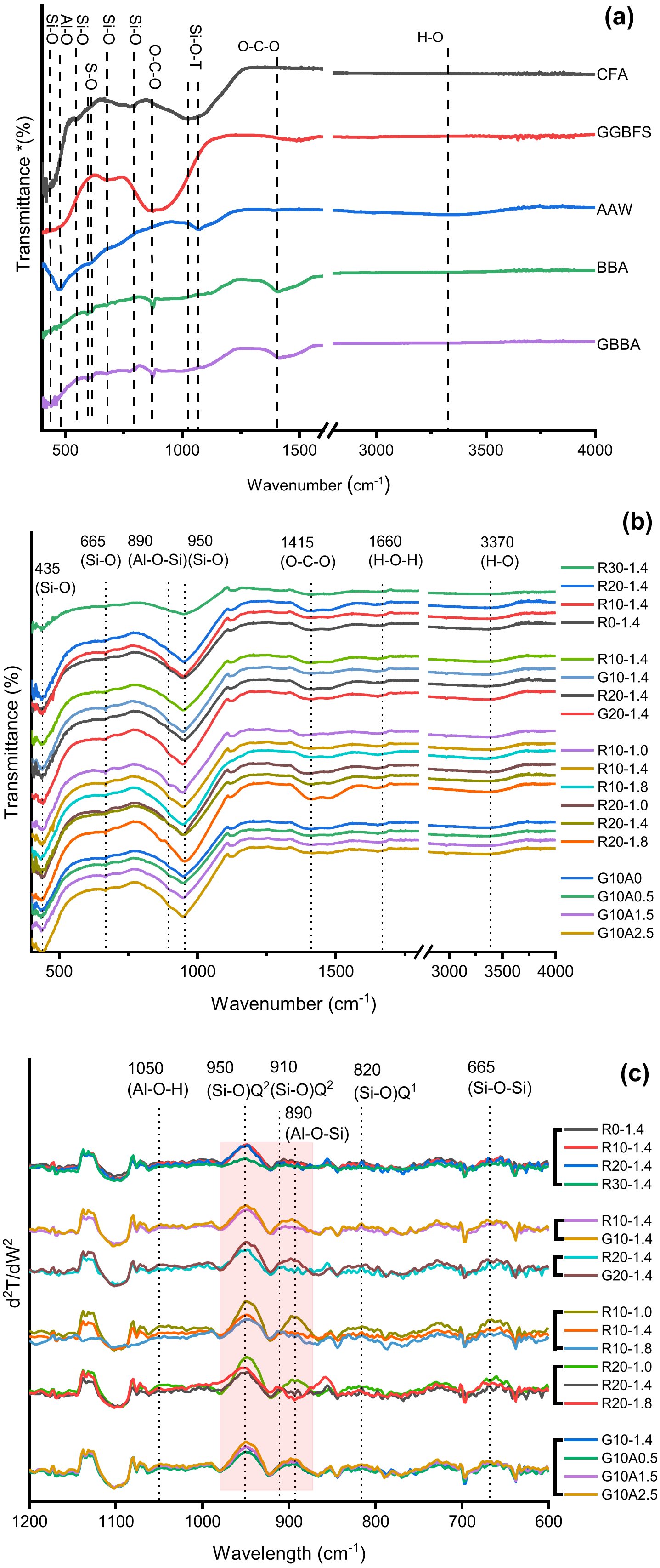

Fig. 5. FT-IR spectra of (a) the raw GGBFS, CFA, BBA, GBBA and AAW, and the 28d samples with various BBA content, fineness, activator modulus and additional AAW: (b): transmittance vs wavelength, (c) 2nd derivative of the transmittance d^2T/dW^2 vs wavelength.

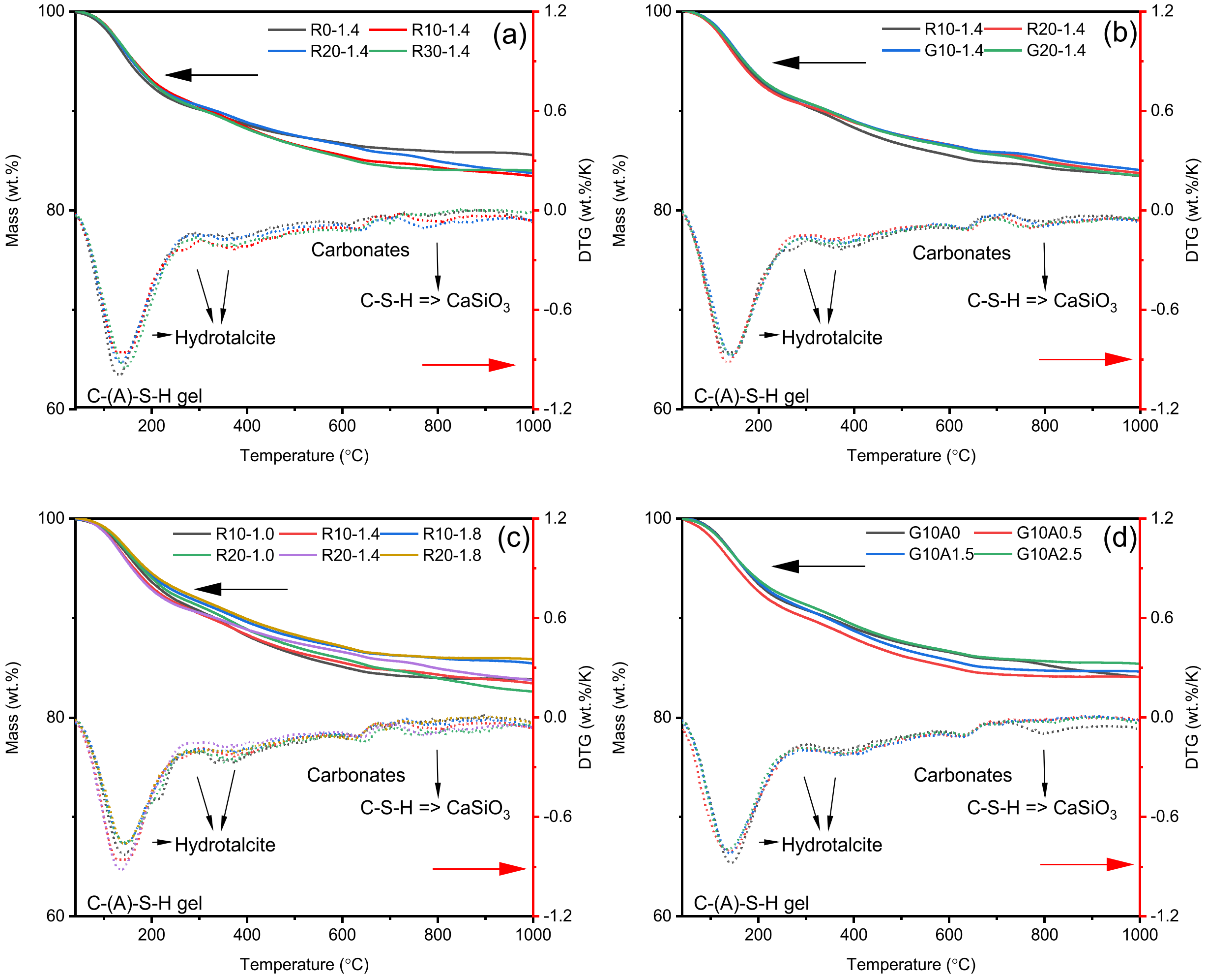

Fig. 6. Thermal analysis of the 28d pastes with different (a-b) BBA/GBBA content, (c) silicate modulus and (d) AAW content.

Table 4
Weight loss (%) at different temperature range in 28d samples.

Group	Weight Loss (%)		
	50–200°C Bound water from C-(A)-S-H gel	250–500°C Bound water from Hydrotalcite-like phases	(40–1000°C) Total weight loss
R0–1.4	8.94	3.51	14.38
R10–1.4	8.54	4.91	16.64
R20–1.4	8.72	4.80	16.33
R30–1.4	8.88	4.61	16.06
R10–1.0	8.08	5.48	16.07
R10–1.8	7.31	4.61	14.55
R20–1.0	7.79	5.16	17.45
R20–1.8	7.05	4.66	14.19
G10–1.4	8.60	4.55	16.04
G20–1.4	8.54	4.71	16.58
G10A0.5	8.94	4.85	15.92
G10A1.5	8.11	5.03	15.44
G10A2.5	7.66	4.66	14.60

BBA leads to their incorporation into C-(A)-S-H gel. Compared with BBA, GBBA has a less significant influence on gel pores, but there is a reduction in capillary pores and the total porosity, particularly evident in the G20–1.4 sample. This indicates that the finer particles act as a filler and refine the pore structure. Furthermore, a higher Ms activator leads to a reduction in capillary pores and the pore size due to the enhanced polymerization, as confirmed by the FT-IR spectra in Fig. 5. In the AAW-modified samples, the porosity of gel pore increases with more AAW, indicating that the dissolved $Al(OH)_4$ participates in the formation of gel products. However, excessive AAW addition also results in a higher content of macro-pores due to the worse workability. Overall, the modifications provide control over the pore size distribution of the matrix. In terms of reducing heavy metals leaching pathways, the use of GBBA and higher Ms activators can help reduce the amount of capillary pores and macro-pores, while increasing Ms and AAW promotes the formation of gel pores.

3.5. Leaching behavior

From an environmental perspective, the leaching behavior of raw materials and BBA-GGBFS-CFA blends were characterized. Table 5 summarizes the leaching values of raw BBA, GBBA, GGBFS, CFA and AAW, with limits established by the Dutch Soil Quality Decree (SQD) regarding the acceptable emissions for inorganic pieces [72]. In the raw BBA and GBBA particles, the leaching contents of chloride (Cl^-), sulphate (SO_4^{2-}), lead (Pb), zinc (Zn), chromium (Cr) and molybdenum (Mo) significantly exceed their legal values, posing a primary concern for their use in building materials. It is noteworthy that GBBA exhibits a higher concentration of heavy metal concentration compared to BBA, indicating that these ions are more easily leached out from the finer particles. Additionally, the contents of Cl^-, SO_4^{2-}, and Cr in AAW, as well as the contents of the Cr and Mo in CFA, surpass the established limits. Therefore, this study focuses on solidifying the aforementioned heavy metals and anions in the BBA-GGBFS-CFA blends.

Table 6 summarizes the leaching contents of Cr, Mo, Zn, Pb, Cl^- and

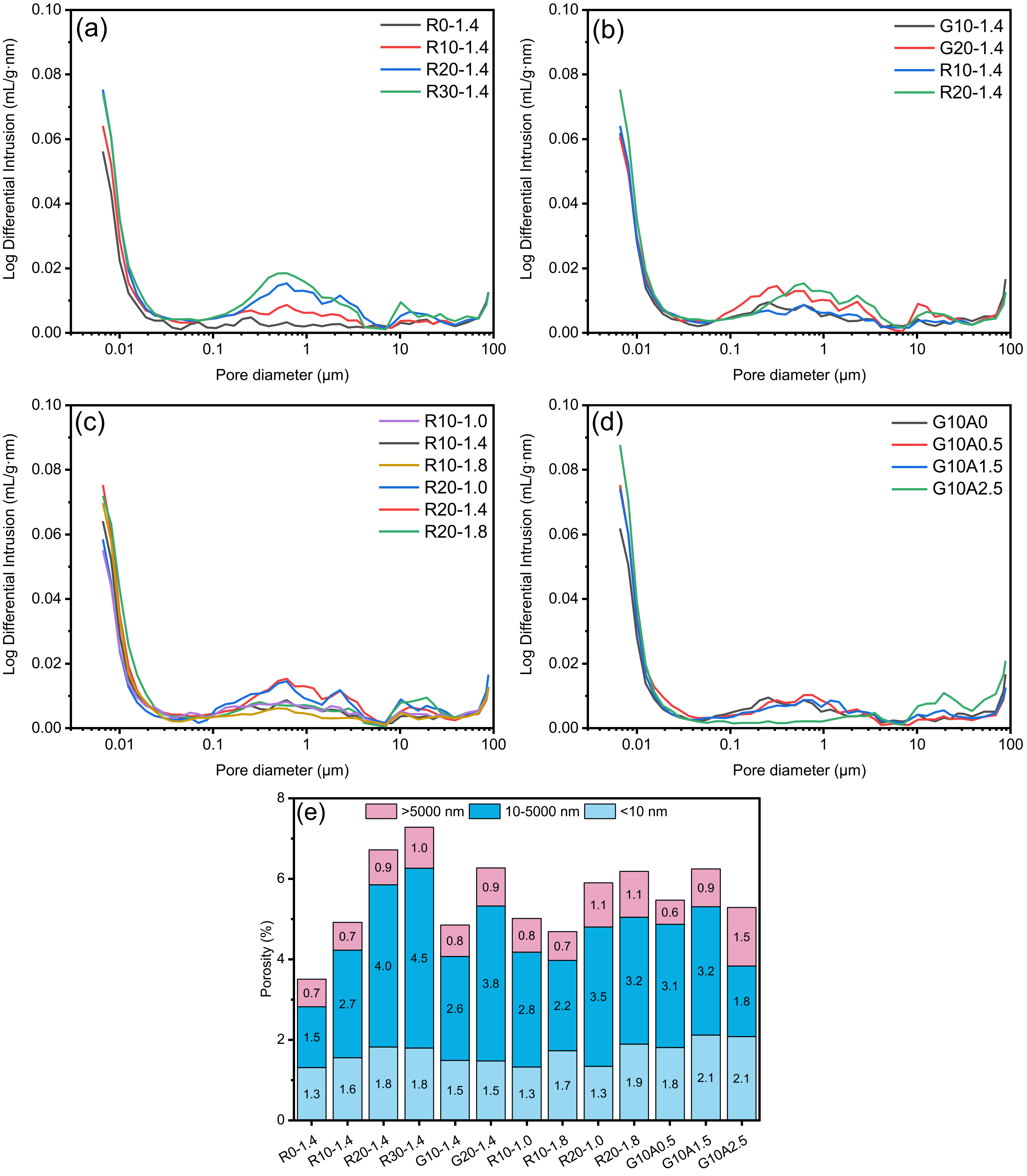

Fig. 7. (a-d) Pore size distribution and (e) Total porosity and the porosity of each type of pores in the prepared 28d pastes with various modifications.

SO_4^{2-} from the 28d BBA-GBFS-CFA blends. A significant reduction in the leaching of heavy metals, chloride and sulfate is evident in all blends. For the leaching of Pb, its concentration falls below detection limits, showcasing remarkably low levels. The notable reduction in Pb leaching has been attributed to its precipitation as silicate species ($PbSiO_3$, Pb_2SiO_4, Pb_3SiO_5), a phenomenon well-established in previous studies [73–75]. Additionally, it has reported that Pb was present in the form of $Pb(OH)_2$ in alkali-activated fly ash/blast furnace slag [76]. Within the BBA-GGBFS-CFA blends, the activators contain abundant silicate ions with high alkalinity, offering substantial capacity to immobilize the leached Pb. Moreover, recent studies have indicated that soluble Pb can be chemically bonded into the amorphous 3D network of the hydrates [16,55].

Concerning the leaching of Zn, its concentration is detectable solely

Table 5
The leaching of BBA and AAW obtained via a one-batch leaching test (mg/kg dry mass of materials).

E/I	BBA	GBBA	AAW	GGBFS	CFA	SQD*
Cl$^-$	**4590**	**4640**	**3490**	406.3	4.85	616
SO$_4^{2-}$	**19270**	**19220**	**69910**	1226	2172	2430
As	UDL	UDL	0.04	UDL	UDL	0.90
Pb	**304.37**	**457.5**	0.12	UDL	UDL	2.30
Zn	**28.95**	**39.59**	0.01	0.14	UDL	4.50
Ba	1.76	3.70	0.05	2.25	15.4	22.0
Cr	**25.39**	**34.63**	**0.79**	0.26	**2.06**	0.63
Cu	0.16	0.35	0.05	UDL	UDL	0.90
Mo	**3.28**	**3.27**	0.17	UDL	**5.28**	1.00
Sb	UDL	UDL	0.04	UDL	UDL	0.32
B	2.85	2.39	45250	0.12	29.7	
Mg	0.03	0.04	13.28	0.19	UDL	
Sr	40.46	43.72	0.73	17.6	45.5	
Na	2430	2480	41280	246.9	255.5	
K	6070	6270	24	128.4	113.7	
Ca	6120	8470	133	1720	993.8	
Al	0.08	0.12	0.46	UDL	0.93	
pH	12.8	12.9	8.4	11.5	11.6	

Note: pH value of the leachate at L/S10, UDL: Under detect limitation <0.02 mg/kg, SQD

[*] Unshaped material as specified by the legislation: Soil Quality Decree [72], E/I: elements or ions, the values in **bold** are above the limits of SQD.

in low Ms activated samples (R10–1.0 and R20–1.0). The lower Ms results in increased alkalinity of the solution [77], contributing to the formation of soluble oxyanionic Zn(OH)$_4^{2-}$ [10]. Consequently, Zn species are not easily immobilized through simple precipitation or ion exchange with alkali cations balancing the negatively charged Al tetrahedra. Overall, a reduction in Zn leaching can be observed, potentially attributed to Zn-bearing phases, such as the $Zn_4Si_2O_7(OH)_2·H_2O$, γ-$Zn(OH)_2$, $CaZn_2(OH)_6·2H_2O$ [78,79]. Unfortunately, these phases could not be detected in the present XRD patterns due to the relatively low Zn concentration. Furthermore, previous studies have confirmed the incorporation of Zn within the matrix of C-S-H [80,81].

Regarding the leaching of Cr, its concentration exhibits an increase with a higher proportion of BBA, since Cr is mainly derived from BBA. The elevated leaching from finer particles of GBBA is understandable, attributing the heightened surface area. However, a lower activator modulus contributes to a reduction in Cr leaching. Several factors may contribute to this observation. Firstly, the promoted formation of hydrotalcite-like phases in samples R10–1.0 and R20–1.0 plays a significant role in diminishing Cr leaching, as it could be incorporated into the hydrotalcite layer framework through isomorphic substitution for Mg and Al ions [82]. Secondly, the high alkalinity induces the precipitation of $Cr(OH)_3$, while the abundant Ca^{2+} promotes the formation of $CaCrO_4$ [83]. The introduction of additional AAW initially reduces Cr leaching, but a further increase in AAW leads to an increase in Cr leaching. This phenomenon can be attributed to the dissolution of AAW, which increases the substitution of [AlO_4] in the silica chain, thereby enhancing the adsorption of Cr. Furthermore, previous studies [84,85] have suggested that boehmite has remarkable adsorption capacity for Cr, indicating that the amorphous boehmite in the AAW used in this study may contributes similarly. However, it is noteworthy that excess AAW reduces the alkalinity of the pore solution, adversely affects workability, and induces more macro-pores (Fig. 7), facilitating the migration of Cr during leaching.

In contrast to Cr, the leached Mo concentration decrease with increasing substitution of BBA, as Mo is mainly sourced from CFA. Compared to BBA, an equivalent amount of GBBA reduces Mo leaching, indicating the positive effect of the increased reactivity of GBBA on the reaction products, as evidenced by the reduced capillary pores (Fig. 7). Moreover, increasing the Ms of activators leads to reduced leaching of Mo. This is due to the lower pH of pore solution, which limits the solubility of Mo [86]. Additionally, the leaching of Mo oxyanions is assumed to be regulated by the dissolution of $CaMoO_4$ [87]. Therefore, a lower pH environment in the pore solution proves advantageous for controlling the leaching of Mo, as a decreased pH leads to a higher concentration of Ca^{2+}. A similar effect is achieved when AAW is added. However, excessive AAW results in adverse leaching of Mo due to the defective encapsulation caused by the increased pore structure (Fig. 7).

The leaching of Cl$^-$ and SO$_4^{2-}$ exhibits an increase with the BBA and GBBA content. This trend is consistent with the leaching behavior observed for Cr$^-$, where BBA serves as the primary source for the leaching of these ions. Nevertheless, the utilization of lower Ms activators leads to an increasing in Cl$^-$ leaching, accompanied by a reduction in SO$_4^{2-}$ leaching in the blends. This observation aligns with findings of Tao et al., who attributed such behavior to the distinct selectivity of hydrotalcite-like phases for SO$_4^{2-}$ ions rather than Cl$^-$ ions [88]. Furthermore, in comparison to G10–1.4, a higher addition of AAW induces a reduction in Cl$^-$ leaching within the blends. Unlike Cl$^-$ leaching, the leaching of SO$_4^{2-}$ initially experiences a decline with the addition of AAW but subsequently increases with further increments in AAW content. The decrease in leached anions can be attributed to the capacity of AAW to promote the formation of additional gel pores (Fig. 7), facilitating the absorption and immobilization of anions within the matrix. However, it is crucial to note that AAW inherently contains leachable sulfate, and augmenting its dosage results in a concurrent elevation in SO$_4^{2-}$ leaching. Overall, Cl$^-$ leaching remains significantly below its respective legal limits. However, substantial concentrations of SO$_4^{2-}$ are notably observed in blends containing 20 wt% BBA/GBBA or higher, surpassing the legal threshold. This occurrence is attributed to the inherent anhydrite content, leading to an increased leachable sulphate. Consequently, addressing the leaching of sulphate in blends with high BBA dosage necessitates further consideration.

It is also noteworthy that the decrease in the leaching level of toxic elements can be partially attributed to the dilution effect, given the relatively lower proportion (10 wt% - 30 wt%) of effective BBA content in the binders. Hence, based on the above findings, it could be concluded that effective solidification of Cr, Mo, Pb, Zn, Cl$^-$ and SO$_4^{2-}$ can be achieved in the BBA-GGBFS-CFA blends through physical encapsulation,

Table 6
The leaching of 28d blends obtained via a one-batch leaching test (mg/kg dry mass of materials).

E/I*	R0-1.4	R10-1.4	R20-1.4	R30-1.4	G10-1.4	G20-1.4	R10-1.0	R10-1.8	R20-1.0	R20-1.8	G10 A0**	G10 A0.5	G10 A1.5	G10 A2.5	Limit
Cr	0.04	0.15	0.2	0.33	0.24	0.33	0.14	0.18	0.19	0.33	0.24	0.15	0.20	0.22	1.0
Mo	0.49	0.44	0.4	0.33	0.38	0.31	0.50	0.44	0.41	0.37	0.38	0.35	0.39	0.42	0.63
Zn	UDL	UDL	UDL	UDL	UDL	UDL	0.09	UDL	0.12	UDL	UDL	UDL	UDL	UDL	4.5
Pb	UDL	UDL	UDL	UDL	UDL	UDL	UDL	UDL	UDL	UDL	UDL	UDL	UDL	UDL	2.3
Cl$^-$	94	165	255	344	185	258	189	161	267	237	185	182	165	144	616
SO$_4^{2-}$	992	1567	**1984**	**2992**	1663	**1987**	1569	1629	**1980**	**2090**	1663	1510	1598	1702	1730
pH	12.36	12.41	12.45	12.46	12.43	12.46	12.50	12.32	12.53	12.36	12.43	12.42	12.40	12.38	-

Note: UDL: Under detect limitation <0.02 mg/kg,

[*] E/I: elements or ions,

[**] G10A0=G10–1.4, the values in **bold** are above the limits of SQD.

dilution, adsorption and precipitation. There are no leaching concerns when applying a 10 wt% BBA substitution in the hybrid blends.

3.6. Mechanical properties

To evaluate the mechanical properties of BBA-GGBFS-CFA blends as a building material, the compressive strength at 7d and 28d was tested, and the results are presented in Fig. 8. The compressive strength exhibits a decrease with BBA substitution in Fig. 8 **(a)**. This decline can be attributed to the relatively larger particle size of BBA, leading to reduced flowability and a lower packing density of the fresh mortar. Furthermore, BBA shows relatively low reactivity, resulting in a weaker matrix with less gel production, which aligns with the observed increase in capillary pores within the matrix. However, GBBA slightly enhances the compressive strength in Fig. 8 **(b)**. This improvement can be partially ascribed to the enhanced flowability, facilitating the expulsion of air voids and reducing capillary pores. The finer particles of GBBA also contribute to a significantly refined packing density of the matrix, as indicated by the observed decrease in the proportion of capillary pores within the matrix. Furthermore, as outlined in Section 3.1, more reactive $[SiO_4]$ and $[AlO_4]$ from GBBA can promote gel formation. Considering the influence of Ms on the blends in Fig. 8 **(c)**, the activator with a higher Ms enhances the 7d compressive strength, regardless of the BBA replacement level. The high Ms activator solution provides more reactive $[SiO_2]$ content, which can be integrated into the silica chain of the C-(A)-S-H gel. Notably, R10–1.0 and R20–1.0 exhibit better 28d compressive strength compared with R10–1.4 and R20–1.4. This enhancement could be attributed to the better hydration of CFA at later stage due to the higher alkalinity in activators. Upon introducing AAW in Fig. 8 **(d)**, the compressive strength decreases with higher AAW dosage. This can be explained by the dissolution of AAW, which consumes alkaline ions and slows down the dissolution process of GGBFS, consequently reducing gel formation, as evidenced by the decreased bound water in the C-(A)-S-H gel (Table 4).

In conclusion, the compressive strength of the hybrid binder ranges from 36.8 MPa to 58.8 MPa at 28 d, making it suitable as a substitute for various type of cement in terms of mechanical performance according to BS EN 192–1. Furthermore, the mechanical property of the blends can be regulated by adjusting the BBA content, fineness, silicate modulus, and the addition of AAW, allowing customization to meet specific construction requirements.

4. Discussions

In an effort to alleviate the environmental repercussions associated with landfill disposal and the substantial quantity of BBA (approximately 10,000 tons in the Netherlands), this study advocated for the utilization of BBA as construction materials, alongside GGBFS and CFA. Several factors, including the BBA content, fineness, silicate modulus of the activator, and the incorporation of additional AAW, were systematically investigated to optimize the solidification of BBA within alkali-activated materials. Studies have indicated that these factors can impact

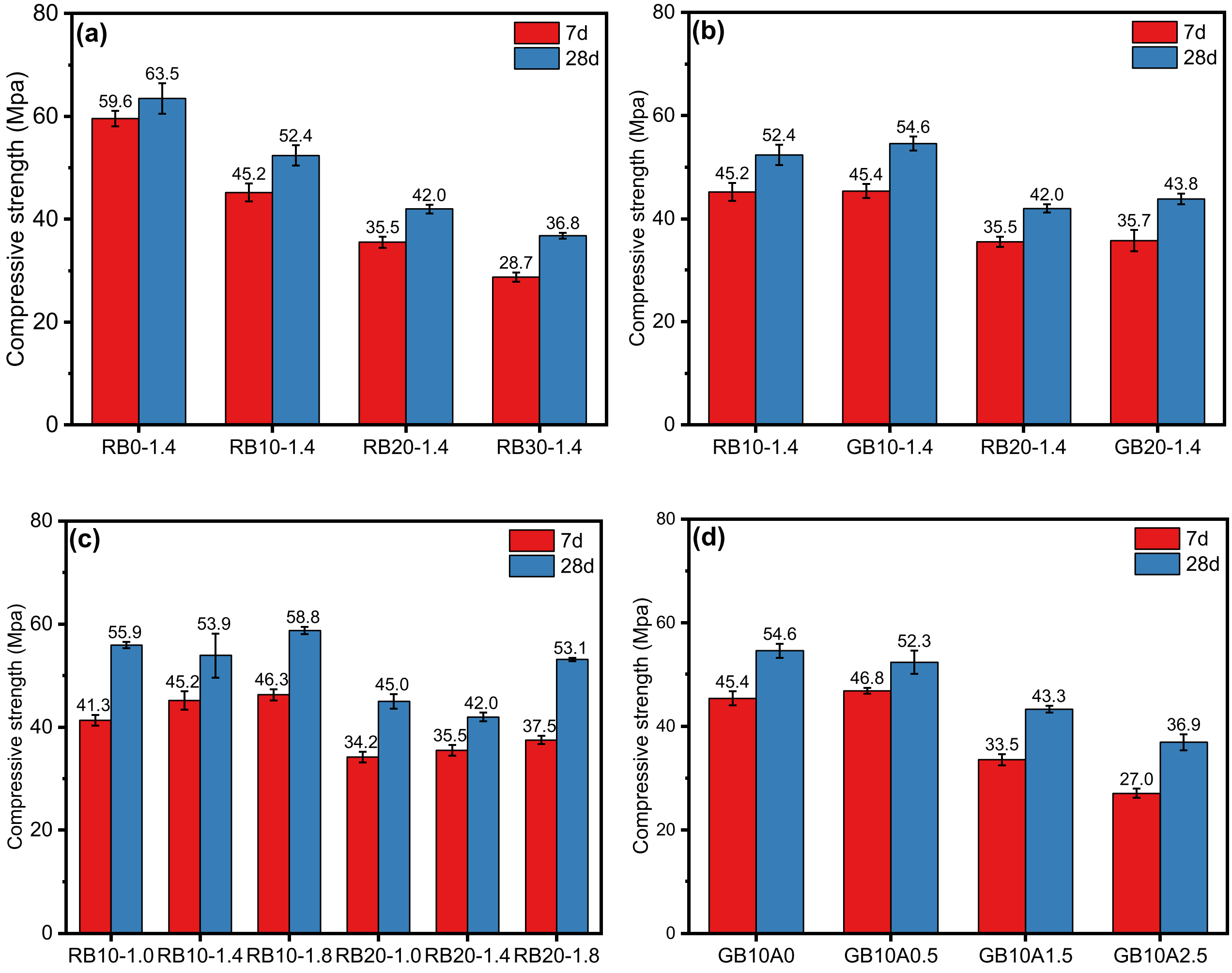

Fig. 8. Compressive strength of all blends at the age of 7d and 28d.

diverse final properties of the hybrid binders, making it unfeasible to achieve optimal performance across all properties with a singular mixing ratio. For instance, a higher modulus contributes to improved mechanical performance but it also associated with higher Cr and sulphate leaching. Hence, optimizing the final properties of hybrid binders is a complex task that cannot solely rely on adjusting a single factor. This study delves into the individual impacts of these factors on the curing properties of hybrid binders to establish a theoretical foundation for practical applications. To clearly provide clarity on these effects, the role of the mentioned factors in influencing the composition of reaction products and pore solutions is further explicated by comparing the variations in the leach solution concerning [$Al(OH)_4^-$], [$Si(OH)_4^-$], [Ca^{2+}], and [Na^+] ions (Fig. 9).

4.1. *The effect of BBA content*

In Fig. 9 **(a)**, the concentration of [$Al(OH)_4^-$], [$Si(OH)_4^-$], [Ca^{2+}], and [Na^+] exhibit a similar trend. Initially, the ion concentrations decrease with a 10 wt% BBA. However, a subsequent increase in the BBA content leads to a higher concentration. This suggests that the 10 wt% BBA optimize each ion in the precipitation of reaction products, consistent with the findings of promoted hydration heat (Fig. 3). The additional BBA mainly provides more Ca^{2+} and Na^+ ions, while having less impact on $Si(OH)_4^-$ ions due its low reactivity, thereby making less contributions in compressive strength (Fig. 8). On the contrary, the irregular shape of BBA particles induces more capillary pores (Fig. 7), resulting in the reduction of the mechanical performance.

4.2. *The effect of BBA fineness*

In Fig. 9 **(b)**, an increase in fineness does elevate the concentration of [$Al(OH)_4^-$], [$Si(OH)_4^-$], [Ca^{2+}], and [Na^+], favoring the formation of reaction products. However, there is minimal growth in [$Si(OH)_4^-$] concentration, suggesting that the improved mechanical properties of G10–1.4 and G20–1.4 are mainly due the filler effect of GBBA, enhancing particle packing and reducing the capillary pores within the binder (Fig. 7). It is crucial to note that the increased fineness induces higher leaching of toxic elements from BBA (Table 6). Additionally, the milling process of BBA incurs higher costs for raw material pretreatment. Hence, the decision to grind BBA should be carefully weighed against the actual budget and performance indicators.

4.3. *The effect of silicate modulus*

Fig. 9 **(c)** illustrates the impact of silicate modulus of the activator on the concentration of [$Al(OH)_4^-$], [$Si(OH)_4^-$], [Ca^{2+}], and [Na^+] in the leachate. The rise in activator modulus correlates with an increased concentration of [$Si(OH)_4^-$], leading to more leachable [$Si(OH)_4^-$] in the pore solution. Interestingly, the concentrations of [$Al(OH)_4^-$], [Ca^{2+}], and [Na^+] exhibit an inverse trend. One potential reason for this

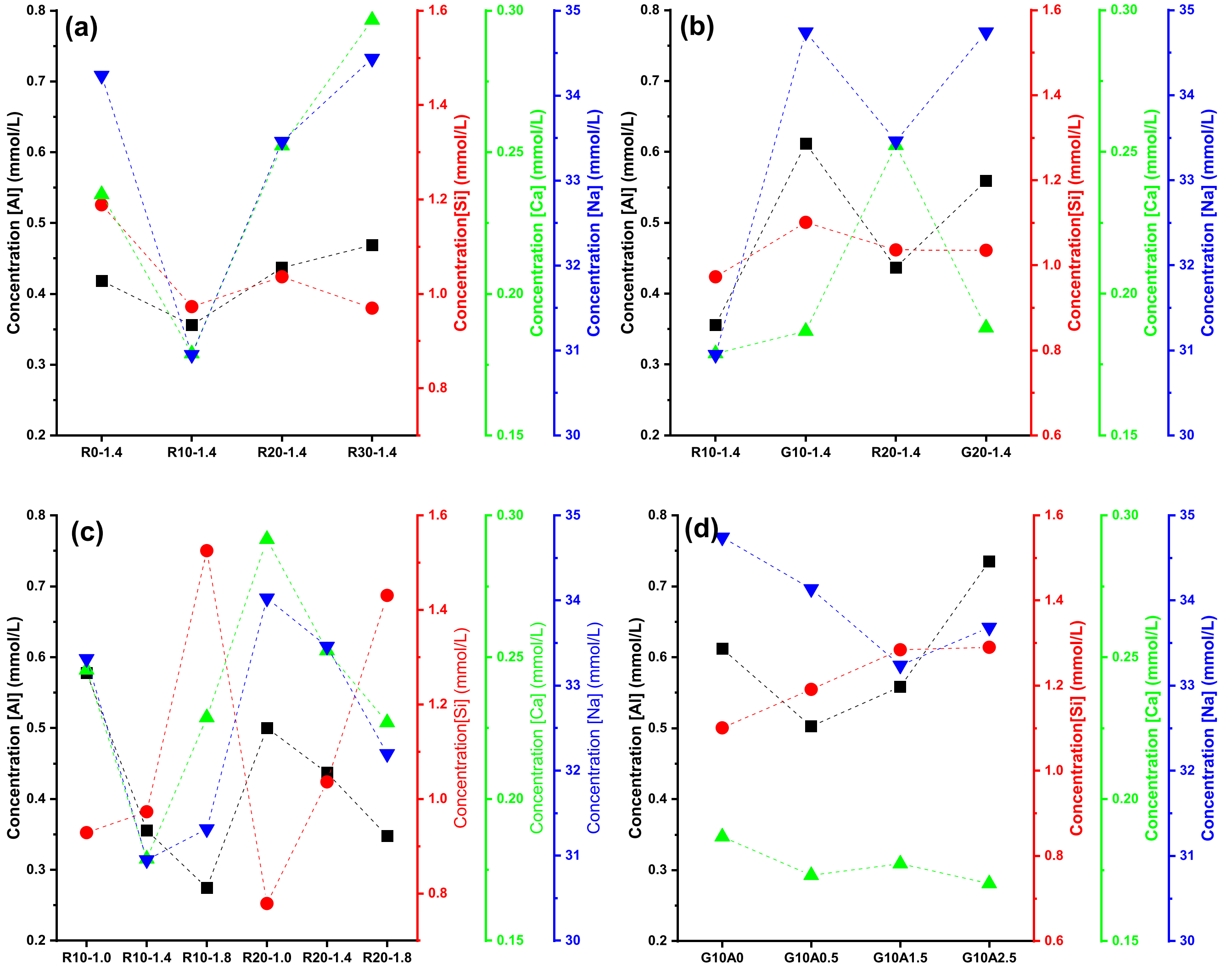

Fig. 9. Cation variation of the leachate from the 28d BBA-GGBFS-CFA blends ([Al], [Si], [Ca],[Na]).

phenomenon is that the ample $[Si(OH)_4^-]$ in R20–1.8 contributes to the consumption of $[Al(OH)_4^-]$, $[Ca^{2+}]$, and $[Na^+]$, forming N/C-(A)-S-H gel. The enhanced production of gel leads to a reduction in capillary pores (Fig. 7), consequently improving the mechanical properties of the binder. Conversely, the insufficient $[Si(OH)_4^-]$ in R20–1.0 results in higher concentrations of $[Al(OH)_4^-]$, $[Ca^{2+}]$, and $[Na^+]$. This promotes the formation of hydrotalcite-like phases, as supported by the higher bound water derived from the hydrotalcite-like phases in TG results (Table 4). The selection of the modulus primarily relies on the desired mechanical properties and leaching performance.

4.4. The effect of additional AAW

The influence of AAW on the concentration of $[Al(OH)_4^-]$, $[Si(OH)_4^-]$, $[Ca^{2+}]$, and $[Na^+]$ in the leachate is summarized in the Fig. 9 **(d)**. The incorporation of AAW leads to a relatively low concentrations of $[Ca^{2+}]$, which may impede the formation of the C-(A)-S-H gel, consistent with the decreased bound water observed in Table 4. This reduction in Ca^{2+} is linked to decreased alkalinity resulting from AAW dissolution, thereby contributing to the deterioration in mechanical performance. On the other hand, the high leaching of B from AAW (Table 5) may contribute to Ca^{2+} consumption through the precipitation of calcium borate ($CaO\cdot3B_2O_3\cdot8H_2O$, $CaO\cdot B_2O_3\cdot6H_2O$) or ulexite ($NaCa[B_5O_6(OH)_6]\cdot5H_2O$) [89]. Despite these effects, the co-disposal objective of BBA and AAW has been achieved, with acceptable leaching behavior and desirable mechanical performance for use as building materials.

5. Conclusion

This work investigates the hydration process in alkali-activated BBA-GGBFS-CFA blended binder and its potential for heavy metal immobilization. The effect of BBA content, BBA fineness, silicate modulus of activator and AAW on reaction kinetics, hydration products, microstructure and mechanical properties of the blends are investigated, as well as the leaching behavior of hybrid binders. The following conclusions can be drawn:

- BBA exhibits lower reactivity compared to CFA but still contains reactive minerals that can form the hydrotalcite-like phases in highly alkaline solution. The dissolution and polymerization of the hybrid blends are enhanced by 10 wt% BBA, as evidenced by a greater cumulative hydration heat release. Main hydration products are the C-(A)-S-H gels, with BBA replacement accelerating reaction process and enhancing gel products.
- The compressive strength of the GGBFS-CFA-BBA blends ranges from 36.8 to 58.8 MPa at 28d, correlating with BBA substitution levels, fineness, silicate modulus and additional AAW, indicating their potential application as building materials.
- The hybrid blends effectively immobilize the high leachable Cl^-, SO_4^{2-}, Cr, Mo, Pb, and Zn content from BBA/GBBA. No heavy metal leaching exceeding the Dutch legal limit occurs within the 10 wt% G/BBA substitution level. However, high SO_4^{2-} leaching needs to be addressed when pursuing higher substitution levels of BBA.
- AAW retards the reaction process of GBBA-GGBFS-CFA blends, leading to strength degradation. However, a low AAW dosage enhances the immobilization efficiency of toxic ions. Co-disposal of AAW and BBA is feasible, exhibiting no new leaching problems and providing sufficient compressive strength for building material use.
- The study offers insights into optimizing hybrid blends for sustainable alkali-activated materials, crucial for solidifying secondary industrial by-products. The proposed waste-to-resource model promotes circular economy principles by utilizing waste-combined AAMs as an alternative to ordinary Portland cement and effectively addresses heavy metals leaching from waste materials.

CRediT authorship contribution statement

Xuan Ling: Writing – original draft, Visualization, Validation, Methodology, Investigation, Formal analysis, Data curation, Conceptualization. **Wei Chen:** Writing – review & editing, Supervision, Conceptualization. **Katrin Schollbach:** Writing – review & editing, Supervision, Methodology, Investigation. **H.J.H. Brouwers:** Writing – review & editing, Supervision, Project administration, Conceptualization.

Declaration of Competing Interest

The authors declare that they have no known competing financial interests or personal relationships that could have appeared to influence the work reported in this paper.

Data Availability

Data will be made available on request.

Acknowledgements

This research was supported by the funding of the China Scholarship Council (No. 201906950015) and the Eindhoven University of Technology. The authors would like to thank Euro Trust Management for the supply of biomass bottom ash and aluminium-anodizing waste.

Appendix A. Supporting information

Supplementary data associated with this article can be found in the online version at doi:10.1016/j.conbuildmat.2024.136408.

References

[1] F. Agrela, M. Cabrera, M.M. Morales, M. Zamorano, M. Alshaaer, Biomass fly ash and biomass bottom ash, in: J. de Brito, F. Agrela (Eds.), New Trends Eco-Efficient Recycl. Concr., Woodhead Publishing, 2019, pp. 23–58, https://doi.org/10.1016/B978-0-08-102480-5.00002-6.
[2] M. Cabrera, A.P. Galvin, F. Agrela, M.D. Carvajal, J. Ayuso, Characterisation and technical feasibility of using biomass bottom ash for civil infrastructures, Constr. Build. Mater. 58 (2014) 234–244, https://doi.org/10.1016/j.conbuildmat.2014.01.087.
[3] R. Melotti, E. Santagata, M. Bassani, M. Salvo, S. Rizzo, A preliminary investigation into the physical and chemical properties of biomass ashes used as aggregate fillers for bituminous mixtures, Waste Manag 33 (2013) 1906–1917, https://doi.org/10.1016/j.wasman.2013.05.015.
[4] I. Obernberger, K. Supancic, Possibilities of ash utilisation from biomass combustion plants, : Proc. 17th Eur. Biomass-.-. Conf. Exhib., Hambg. (2009).
[5] J. Cuenca, J. Rodríguez, M. Martín-morales, Z. Sánchez-roldán, M. Zamorano, Effects of olive residue biomass fly ash as filler in self-compacting concrete, Constr. Build. Mater. 40 (2013) 702–709, https://doi.org/10.1016/j.conbuildmat.2012.09.101.
[6] J. Rosales, M. Cabrera, M.G. Beltrán, M. López, F. Agrela, Effects of treatments on biomass bottom ash applied to the manufacture of cement mortars, J. Clean. Prod. 154 (2020) 424–435, https://doi.org/10.1016/j.jclepro.2017.04.024.
[7] M.J.R. Hinojosa, A.P. Galvín, F. Agrela, M. Perianes, A. Barbudo, Potential use of biomass bottom ash as alternative construction material: Conflictive chemical parameters according to technical regulations, FUEL 128 (2014) 248–259, https://doi.org/10.1016/j.fuel.2014.03.017.
[8] M.G. Beltrán, F. Agrela, A. Barbudo, J. Ayuso, A. Ramírez, Mechanical and durability properties of concretes manufactured with biomass bottom ash and recycled coarse aggregates, Constr. Build. Mater. 72 (2014) 231–238, https://doi.org/10.1016/j.conbuildmat.2014.09.019.
[9] M. Cabrera, A.P. Galvin, F. Agrela, M.G. Beltran, J. Ayuso, Reduction of leaching impacts by applying biomass bottom ash and recycled mixed aggregates in structural layers of roads, Mater. (Basel) 9 (2016) 228, https://doi.org/10.3390/ma9040228.
[10] B.I. El-eswed, Chemical evaluation of immobilization of wastes containing Pb, Cd, Cu and Zn in alkali-activated materials: a critical review, J. Environ. Chem. Eng. 8 (2020) 104194, https://doi.org/10.1016/j.jece.2020.104194.
[11] R.A. Antunes, B. Santa, C. Soares, H.G. Riella, Geopolymers with a high percentage of bottom ash for solidification / immobilization of different toxic metals, J. Hazard. Mater. 318 (2016) 145–153, https://doi.org/10.1016/j.jhazmat.2016.06.059.

[12] Y. Luna, X. Querol, D. Antenucci, J. Vale, Waste stabilization / solidification of an electric arc furnace dust using fly ash-based geopolymers, Fuel 88 (2009) 1185–1193, https://doi.org/10.1016/j.fuel.2008.01.021.

[13] X. Chen, Y. Guo, S. Ding, H. Zhang, F. Xia, J. Wang, Utilization of red mud in geopolymer-based pervious concrete with function of adsorption of heavy metal ions, J. Clean. Prod. 207 (2019) 789–800, https://doi.org/10.1016/j.jclepro.2018.09.263.

[14] Q. Tian, S. Nakama, K. Sasaki, Immobilization of cesium in fly ash-silica fume based geopolymers with different Si/Al molar ratios, Sci. Total Environ. 687 (2019) 1127–1137, https://doi.org/10.1016/j.scitotenv.2019.06.095.

[15] Z. Wang, Y. Chen, L. Xu, Z. Zhu, Y. Zhou, F. Pan, K. Wu, Insight into the local C-S-H structure and its evolution mechanism controlled by curing regime and Ca/Si ratio, Constr. Build. Mater. 333 (2022) 127388, https://doi.org/10.1016/j.conbuildmat.2022.127388.

[16] B. Guo, D. Pan, B. Liu, A.A. Volinsky, M. Fincan, J. Du, S. Zhang, Immobilization mechanism of Pb in fly ash-based geopolymer, Constr. Build. Mater. 134 (2017) 123–130, https://doi.org/10.1016/j.conbuildmat.2016.12.139.

[17] J. Chen, Y. Wang, H. Wang, S. Zhou, H. Wu, Detoxification / immobilization of hexavalent chromium using metakaolin-based geopolymer coupled with ferrous chloride, J. Environ. Chem. Eng. 4 (2016) 2084–2089, https://doi.org/10.1016/j.jece.2016.03.038.

[18] Z. Zheng, Y. Li, Z. Zhang, X. Ma, The impacts of sodium nitrate on hydration and microstructure of Portland cement and the leaching behavior of Sr2+, J. Hazard. Mater. 388 (2020) 121805 https://doi.org/10.1016/j.jhazmat.2019.121805.

[19] Y. Zhu, Z. Zheng, Y. Deng, C. Shi, Z. Zhang, Advances in immobilization of radionuclide wastes by alkali activated cement and related materials, Cem. Concr. Compos. 126 (2022) 104377, https://doi.org/10.1016/j.cemconcomp.2021.104377.

[20] X. Gao, Q.L. Yu, H.J.H. Brouwers, Reaction kinetics, gel character and strength of ambient temperature cured alkali activated slag-fly ash blends, Constr. Build. Mater. 80 (2015) 105–115, https://doi.org/10.1016/j.conbuildmat.2015.01.065.

[21] S. Chithiraputhiran, N. Neithalath, Isothermal reaction kinetics and temperature dependence of alkali activation of slag, fly ash and their blends, Constr. Build. Mater. 45 (2013) 233–242, https://doi.org/10.1016/j.conbuildmat.2013.03.061.

[22] Z. Shi, C. Shi, S. Wan, Z. Zhang, Effects of alkali dosage and silicate modulus on alkali-silica reaction in alkali-activated slag mortars, Cem. Concr. Res. 111 (2018) 104–115, https://doi.org/10.1016/J.CEMCONRES.2018.06.005.

[23] W. Zhang, X. Yao, T. Yang, Z. Zhang, Effect of calcined dolomite addition on sodium carbonate-activated slag cements with different curing methods, Adv. Cem. Res. 31 (2019) 370–381, https://doi.org/10.1680/jadcr.17.00204.

[24] X. Ke, S.A. Bernal, J.L. Provis, Controlling the reaction kinetics of sodium carbonate-activated slag cements using calcined layered double hydroxides, Cem. Concr. Res. 81 (2016) 24–37, https://doi.org/10.1016/j.cemconres.2015.11.012.

[25] M. Komljenoć, Z. Baščarević, V. Bradić, Mechanical and microstructural properties of alkali-activated fly ash geopolymers, J. Hazard. Mater. 181 (2010) 35–42, https://doi.org/10.1016/j.jhazmat.2010.04.064.

[26] A. Correia, T. Chambino, L. Gonçalves, A. Franco, R. Gonçalves, A. Gonçalves, V. Limpo, F. Delmas, C. Nogueira, F. Bartolomeu, Municipal wastewater treatment with anodizing solid waste, Desalination 185 (2005) 341–350, https://doi.org/10.1016/j.desal.2005.04.043.

[27] E.M.M. Ewais, N.H.A. Besisa, A. Ahmed, Aluminum titanate based ceramics from aluminum sludge waste, Ceram. Int. 43 (2017) 10277–10287, https://doi.org/10.1016/j.ceramint.2017.05.057.

[28] M.J. Ribeiro, S. Blackburn, J.A. Labrincha, Single screw extrusion of mullite-based tubes containing Al-rich anodising sludge, Ceram. Int. 35 (2009) 1095–1101, https://doi.org/10.1016/j.ceramint.2008.04.024.

[29] J. Corker, I. Marques, S. Resalati, T. Okoroafor, A. Maalouf, Z. Fu, M. Fan, Al-rich industrial waste as new alternative of fumed silica for the manufacture of vacuum insulation panels for building energy conservation, J. Clean. Prod. 415 (2023), https://doi.org/10.1016/j.jclepro.2023.137854.

[30] G.G. de Moraes, B.G. Oliveira, C. Siligardi, M.D. de, M. Innocentini, A.A. M. Oliveira Jr., J.B.R. Neto, D. Hotza, A.P.N. de Oliveira, Production of foundry filters using Al2O3 from the Al-anodizing process, Adv, Sci. Technol. 62 (2010) 119–124, https://doi.org/10.4028/www.scientific.net/ast.62.119.

[31] I. Marques, V. Neto, I. Grilo, M. Vieira, E. Júlio, Recycling of residual sludge from aluminium anodizing and lacquering in clay brinks - a case study of portuguese industries, Cincos 12 (2012) 249–255.

[32] M.T. Souza, L. Onghero, W.L. Repette, F. Raupp Pereira, A.P.N. de Oliveira, Sustainable cement with Al-anodizing waste: evaluating reactivity and feasibility as a shrinkage-compensating admixture, J. Build. Eng. 30 (2020) 101233, https://doi.org/10.1016/j.jobe.2020.101233.

[33] A. Rungchet, P. Chindaprasirt, S. Wansom, K. Pimraksa, Hydrothermal synthesis of calcium sulfoaluminate e belite cement from industrial waste materials, J. Clean. Prod. 115 (2016) 273–283, https://doi.org/10.1016/j.jclepro.2015.12.068.

[34] E.B. da Costa, E.D. Rodríguez, S.A. Bernal, J.L. Provis, L.A. Gobbo, A.P. Kirchheim, Production and hydration of calcium sulfoaluminate-belite cements derived from aluminium anodising sludge, Constr. Build. Mater. 122 (2016) 373–383, https://doi.org/10.1016/j.conbuildmat.2016.06.022.

[35] O.M. Jensen, Thermodynamic limitation of self-desiccation, Cem. Concr. Res. 25 (1995) 157–164, https://doi.org/10.1016/0008-8846(94)00123-G.

[36] C. Ma, B. Chen, L. Chen, Effect of organic matter on strength development of self-compacting earth-based construction stabilized with cement-based composites, Constr. Build. Mater. 123 (2016) 414–423, https://doi.org/10.1016/j.conbuildmat.2016.07.018.

[37] X. Gao, Q.L. Yu, H.J.H. Brouwers, Assessing the porosity and shrinkage of alkali activated slag-fly ash composites designed applying a packing model, Constr. Build. Mater. 119 (2016) 175–184, https://doi.org/10.1016/j.conbuildmat.2016.05.026.

[38] X. Gao, Q.L. Yu, H.J.H. Brouwers, Properties of alkali activated slag-fly ash blends with limestone addition, Cem. Concr. Compos. 59 (2015) 119–128, https://doi.org/10.1016/j.cemconcomp.2015.01.007.

[39] T. Williamson, M.C.G. Juenger, The role of activating solution concentration on alkali – silica reaction in alkali-activated fly ash concrete, Cem. Concr. Res. 83 (2016) 124–130, https://doi.org/10.1016/j.cemconres.2016.02.008.

[40] A. Fernández-Jiménez, Á. Palomo, T. Vazquez, R. Vallepu, T. Terai, K. Ikeda, Alkaline activation of blends of metakaolin and calcium aluminate, J. Am. Ceram. Soc. 91 (2008) 1231–1236, https://doi.org/10.1111/j.1551-2916.2007.02002.x.

[41] Y. Luo, K.M. Klima, H.J.H. Brouwers, Q. Yu, Effects of ladle slag on Class F fly ash geopolymer: reaction mechanism and high temperature behavior, Cem. Concr. Compos. 129 (2022) 104468, https://doi.org/10.1016/j.cemconcomp.2022.104468.

[42] S. Barzgar, M. Tarik, C. Ludwig, B. Lothenbach, The effect of equilibration time on Al uptake in C-S-H, Cem. Concr. Res. 144 (2021) 106438, https://doi.org/10.1016/j.cemconres.2021.106438.

[43] E. Bernard, B. Lothenbach, D. Rentsch, I. Pochard, A. Dauzères, Formation of magnesium silicate hydrates (M-S-H), Phys. Chem. Earth 99 (2017) 142–157, https://doi.org/10.1016/j.pce.2017.02.005.

[44] H. Grénman, T. Salmi, D.Yu, J. Addai-mensah, Dissolution of boehmite in sodium hydroxide at ambient pressure: kinetics and modelling, Hydrometallurgy 102 (2010) 22–30, https://doi.org/10.1016/j.hydromet.2010.01.005.

[45] M. Tramontin, L. Simão, O. Rubem, K. Montedo, F. Raupp, A. Pedro, N. De Oliveira, Aluminum anodizing waste and its uses: an overview of potential applications and market opportunities, Waste Manag 84 (2019) 286–301, https://doi.org/10.1016/j.wasman.2018.12.003.

[46] E. Deir, B.S. Gebregziabiher, S. Peethamparan, Influence of starting material on the early age hydration kinetics, microstructure and composition of binding gel in alkali activated binder systems, Cem. Concr. Compos. 48 (2014) 108–117, https://doi.org/10.1016/j.cemconcomp.2013.11.010.

[47] E. Najafi Kani, A. Allahverdi, J.L. Provis, Calorimetric study of geopolymer binders based on natural pozzolan, J. Therm. Anal. Calorim. 127 (2017) 2181–2190, https://doi.org/10.1007/s10973-016-5850-7.

[48] T. Luukkonen, H. Sreenivasan, Z. Abdollahnejad, J. Yliniemi, A. Kantola, V. V. Telkki, P. Kinnunen, M. Illikainen, Influence of sodium silicate powder silica modulus for mechanical and chemical properties of dry-mix alkali-activated slag mortar, Constr. Build. Mater. 233 (2020) 117354, https://doi.org/10.1016/j.conbuildmat.2019.117354.

[49] X. Ling, K. Schollbach, G. Liu, H.J.H. Brouwers, The utilization of waste incineration filter dust (WIFD) in sodium carbonate activated slag mortars, Constr. Build. Mater. 313 (2021) 125494, https://doi.org/10.1016/j.conbuildmat.2021.125494.

[50] E. Kapeluszna, Ł. Kotwica, A. Różycka, Ł. Gołek, Incorporation of Al in C-A-S-H gels with various Ca/Si and Al/Si ratio: microstructural and structural characteristics with DTA/TG, XRD, FTIR and TEM analysis, Constr. Build. Mater. 155 (2017) 643–653, https://doi.org/10.1016/j.conbuildmat.2017.08.091.

[51] T. Schade, F. Bellmann, B. Middendorf, Quantitative analysis of C-(K)-A-S-H-amount and hydrotalcite phase content in finely ground highly alkali-activated slag/silica fume blended cementitious material, Cem. Concr. Res. 153 (2022) 106706, https://doi.org/10.1016/j.cemconres.2021.106706.

[52] P. Koilraj, Y. Kamura, K. Sasaki, Synergetic co-immobilization of SeO4 2- and Sr2+ from aqueous solution onto multifunctional graphene oxide and carbon-dot based layered double hydroxide nanocomposites and their mechanistic investigation, J. Mater. Chem. A. 6 (2018) 10008–10018, https://doi.org/10.1039/c8ta01605d.

[53] H. Asiabi, Y. Yamini, M. Shamsayei, Highly selective and efficient removal of arsenic(V), chromium(VI) and selenium(VI) oxyanions by layered double hydroxide intercalated with zwitterionic glycine, J. Hazard. Mater. 339 (2017) 239–247, https://doi.org/10.1016/j.jhazmat.2017.06.042.

[54] N.D.M. Evans, Binding mechanisms of radionuclides to cement, Cem. Concr. Res. 38 (2008) 543–553, https://doi.org/10.1016/j.cemconres.2007.11.004.

[55] G. Qiao, D. Hou, W. Li, B. Yin, Y. Zhang, P. Wang, Molecular insights into migration of heavy metal ion in calcium silicate hydrate (CSH) surface and intra-CSH (Ca / Si = 1. 3, Constr. Build. Mater. 365 (2023) 130097, https://doi.org/10.1016/j.conbuildmat.2022.130097.

[56] P. Rovnaník, P. Bayer, P. Rovnaníková, Characterization of alkali activated slag paste after exposure to high temperatures, Constr. Build. Mater. 47 (2013) 1479–1487, https://doi.org/10.1016/j.conbuildmat.2013.06.070.

[57] X. Gao, Q.L. Yu, H.J.H. Brouwers, Reaction kinetics, gel character and strength of ambient temperature cured alkali activated slag–fly ash blends, Constr. Build. Mater. 80 (2015) 105–115, https://doi.org/10.1016/J.CONBUILDMAT.2015.01.065.

[58] M. Criado, A. Palomo, A. Ferna, Alkali activation of fly ashes. Part 1: Effect of curing conditions on the carbonation of the reaction products, Fuel 84 (2005) 2048–2054, https://doi.org/10.1016/j.fuel.2005.03.030.

[59] S.A. Bernal, J.L. Provis, V. Rose, R. Mejía De Gutierrez, Evolution of binder structure in sodium silicate-activated slag-metakaolin blends, Cem. Concr. Compos. 33 (2011) 46–54, https://doi.org/10.1016/j.cemconcomp.2010.09.004.

[60] P. Yu, R.J. Kirkpatrick, B. Poe, P.F. McMillan, X. Cong, Structure of Calcium Silicate Hydrate (C-S-H): Near-, Mid-, and Far-Infrared Spectroscopy, J. Am. Ceram. Soc. 82 (1999) 742–748.

[61] L. Fernandez, C. Alonso, A. Hidalgo, C. Andrade, The role of magnesium during the hydration of C3S and C-S-H formation. Scanning electron microscopy and mid-infrared studies, Adv. Cem. Res. 17 (2005) 9–21, https://doi.org/10.1680/adcr.2005.17.1.9.

[62] J. Higl, D. Hinder, C. Rathgeber, B. Ramming, M. Lindén, Detailed in situ ATR-FTIR spectroscopy study of the early stages of C-S-H formation during hydration of monoclinic C3S, Cem. Concr. Res. 142 (2021), https://doi.org/10.1016/j.cemconres.2021.106367.

[63] A. Vidmer, G. Sclauzero, A. Pasquarello, Infrared spectra of jennite and tobermorite from first-principles, Cem. Concr. Res. 60 (2014) 11–23, https://doi.org/10.1016/j.cemconres.2014.03.004.

[64] N.Y. Mostafa, A.A. Shaltout, H. Omar, S.A. Abo-El-Enein, Hydrothermal synthesis and characterization of aluminium and sulfate substituted 1.1 nm tobermorites, J. Alloy. Compd. 467 (2009) 332–337, https://doi.org/10.1016/j.jallcom.2007.11.130.

[65] J. Partyka, M. Les, Raman and infrared spectroscopy study on structure and microstructure of glass – ceramic materials from SiO2–Al2O3–Na2O–K2O–CaO system modified by variable molar ratio of SiO2/Al2O3, Spectrochim. Acta Part A Mol. Biomol. Spectrosc. Biomol. Spectrosc. 152 (2016) 82–91, https://doi.org/10.1016/j.saa.2015.07.045.

[66] M.Ben Haha, B. Lothenbach, G. Le Saout, F. Winnefeld, Influence of slag chemistry on the hydration of alkali-activated blast-furnace slag - Part II: Effect of Al2O3, Cem. Concr. Res. 42 (2012) 74–83, https://doi.org/10.1016/j.cemconres.2011.08.005.

[67] H.A. Abdel Gawwad, S. Abd El-Aleem, A.S. Ouda, Preparation and characterization of one-part non-Portland cement, Ceram. Int. 42 (2016) 220–228, https://doi.org/10.1016/j.ceramint.2015.08.096.

[68] M. Ben Haha, G. Le Saout, F. Winnefeld, B. Lothenbach, Influence of activator type on hydration kinetics, hydrate assemblage and microstructural development of alkali activated blast-furnace slags, Cem. Concr. Res. 41 (2011) 301–310, https://doi.org/10.1016/j.cemconres.2010.11.016.

[69] R.J. Myers, E. L'Hôpital, J.L. Provis, B. Lothenbach, Effect of temperature and aluminium on calcium (alumino)silicate hydrate chemistry under equilibrium conditions, Cem. Concr. Res. 68 (2015) 83–93, https://doi.org/10.1016/j.cemconres.2014.10.015.

[70] K. Scrivener, R. Snellings, B. Lothenbach, A practical guide to microstructural analysis of cementitious materials, Crc Press Boca Raton, FL, USA, 2016, https://doi.org/10.1201/b19074.

[71] J. Liu, N. Farzadnia, C. Shi, Microstructural and micromechanical characteristics of ultra-high performance concrete with superabsorbent polymer (SAP), Cem. Concr. Res. 149 (2021) 106560, https://doi.org/10.1016/j.cemconres.2021.106560.

[72] Soil Quality Decree, The Soil Quality Regulation, 2009. 〈https://rwsenvironment.eu/subjects/soil/legislation-and/soil-quality-decree/〉.

[73] C.E. Halim, S.A. Short, J.A. Scott, R. Amal, G. Low, Modelling the leaching of Pb, Cd, As, and Cr from cementitious waste using PHREEQC, J. Hazard. Mater. 125 (2005) 45–61, https://doi.org/10.1016/j.jhazmat.2005.05.046.

[74] J. Zhang, J.L. Provis, D. Feng, J.S.J. Van Deventer, Geopolymers for immobilization of Cr6+, Cd2+, and Pb2+, J. Hazard. Mater. 157 (2008) 587–598, https://doi.org/10.1016/j.jhazmat.2008.01.053.

[75] A. Palomo, M. Palacios, Alkali-activated cementitious materials: Alternative matrices for the immobilisation of hazardous wastes Part II. Stabilisation of chromium and lead, Cem. Concr. Res. 33 (2003) 289–295.

[76] J. Koplík, L. Kalina, The characterization of fixation of Ba, Pb, and Cu in alkali-activated fly ash / blast furnace slag matrix, Mater. (Basel) 9 (2016) 533, https://doi.org/10.3390/ma9070533.

[77] X. Gao, Q.L. Yu, A. Lazaro, H.J.H. Brouwers, Investigation on a green olivine nano-silica source based activator in alkali activated slag-fly ash blends: Reaction kinetics, gel structure and carbon footprint, Cem. Concr. Res. 100 (2017) 129–139, https://doi.org/10.1016/j.cemconres.2017.06.007.

[78] F. Ziegler, A.M. Scheidegger, C.A. Johnson, R. Dähn, E. Wieland, Sorption mechanisms of zinc to calcium silicate hydrate: X-ray Absorption Fine Structure (XAFS) investigation 35 (2001) 1550–1555.

[79] J. Tan, Z. Sierens, B. Vandevyvere, H. Dan, J. Li, Zinc oxide in alkali-activated slag (AAS): retardation mechanism, reaction kinetics and immobilization, Constr. Build. Mater. 371 (2023) 130739, https://doi.org/10.1016/j.conbuildmat.2023.130739.

[80] C.E. Tommaseo, M. Kersten, Aqueous solubility diagrams for cementitious waste stabilization systems. 3. Mechanism of zinc immobilizaton by calcium silicate hydrate, Environ. Sci. Technol. 36 (2002) 2919–2925.

[81] I. Moulin, A. Masion, P.M. Bertsch, M.R. Wiesner, J. Bottero, F. Mosnier, C. Haehnel, X-ray absorption spectroscopy study of immobilization processes for heavy metals in calcium silicate hydrates. 2. Zinc, Langmuir 17 (2001) 3658–3665.

[82] B. Li, S. Zhang, Q. Li, N. Li, B. Yuan, W. Chen, H.J.H. Brouwers, Q. Yu, Uptake of heavy metal ions in layered double hydroxides and applications in cementitious materials: Experimental evidence and first-principle study, Constr. Build. Mater. 222 (2019) 96–107, https://doi.org/10.1016/j.conbuildmat.2019.06.135.

[83] D. Wang, Q. Wang, S. Zhuang, J. Yang, Evaluation of alkali-activated blast furnace ferronickel slag as a cementitious material: Reaction mechanism, engineering properties and leaching behaviors, Constr. Build. Mater. 188 (2018) 860–873, https://doi.org/10.1016/j.conbuildmat.2018.08.182.

[84] W. Cui, X. Zhang, C.I. Pearce, M.H. Engelhard, H. Zhang, Y. Wang, S.M. Heald, S. Zheng, Y. Zhang, S.B. Clark, P. Li, Z. Wang, K.M. Rosso, Effect of Cr(III) Adsorption on the Dissolution of Boehmite Nanoparticles in Caustic Solution, Environ. Sci. Technol. 54 (2020) 6375–6384, https://doi.org/10.1021/acs.est.9b07881.

[85] J. Li, M. Li, X. Yang, Y. Zhang, X. Liu, F. Liu, Morphology-controlled synthesis of boehmite with enhanced efficiency for the removal of aqueous Cr(VI) and nitrates, Nanotechnology 30 (2019).

[86] M. Izquierdo, X. Querol, Leaching behaviour of elements from coal combustion fly ash: an overview, Int. J. Coal Geol. 94 (2012) 54–66, https://doi.org/10.1016/j.coal.2011.10.006.

[87] Q. Alam, M.V.A. Florea, K. Schollbach, H.J.H. Brouwers, A two-stage treatment for Municipal Solid Waste Incineration (MSWI) bottom ash to remove agglomerated fine particles and leachable contaminants, Waste Manag 67 (2020) 181–192, https://doi.org/10.1016/j.wasman.2017.05.029.

[88] T. Liu, S. Li, Y. Chen, H.J.H. Brouwers, Q. Yu, In-situ formation of layered double hydroxides in MgO – NaAlO2-activated GGBS / MSWI BA: Impact of Mg2 + on reaction mechanism and leaching behavior, Cem. Concr. Compos. 140 (2023) 105114, https://doi.org/10.1016/j.cemconcomp.2023.105114.

[89] W. Chen, X. Ling, Q. Li, B. Yuan, B. Li, H. Ma, Experimental evidence on formation of ulexite in sulfoaluminate cement paste mixed with high concentration borate solution and its retarding effects, Constr. Build. Mater. 215 (2019) 777–785, https://doi.org/10.1016/j.conbuildmat.2019.04.242.